Founded 1925

Incorporated
by Royal Charter 1961

"To promote the advancement of radio, electronics and kindred subjects by the exchange of information in these branches of engineering.

VOLUME 42 No. 8 AUGUST 1972

THE RADIO AND ELECTRONIC ENGINEER

The Journal of the Institution of Electronic and Radio Engineers

Framework for Government Research and Development

THE 'Green Paper' on Government Research and Development published last November* containing the rather divergent proposals of the Head of the Central Policy Review Staff, Lord Rothschild, F.R.S., and of a Group appointed by the Council for Scientific Policy under the Chairmanship of Sir Frederick Dainton, F.R.S., invited comment from the scientific community. The subsequent 'White Paper'† acknowledges that it was helped by wide ranging observations and consultations, but one must conclude after re-reading the preamble to the Green Paper, that the Government's decisions had already been made, for only in a small measure have the recommendations of the evidently favoured 'Rothschild' report been modified.

It will be recalled‡ that Lord Rothschild's thesis had called for the adoption in civil R & D of the 'customer/contractor' principle already applied for defence R & D, which views the Departments as customers, and the Research Councils as contractors. Cautious agreement with this principle has been expressed by such bodies as the Royal Society, the Council of Engineering Institutions and the National Electronics Council: however, the validity of the approach for pure or basic research has been widely questioned. It seems doubtful that the Government's acceptance of a general research surcharge on customer's programmes, which will vary and will be settled by Departments in agreement with the Treasury, will allay these misgivings.

The transference of sums allocated to R & D from the control of three of the Research Councils (Agriculture, Medical and Natural Environment) to the customer Departments is another controversial aspect. Despite a reduction of the total transfer from the £27M per annum suggested by Lord Rothschild to £20M per annum by 1975–6 (out of a current total of £56·4M per annum), this will still be regarded as threatening the support that can be given to the universities. The Science Research Council has a budget as large as the A.R.C., M.R.C. and N.E.R.C. together and its funding is at present to be left unchanged. This is because the S.R.C.'s primary purpose is to sustain standards of education and research in the universities and to make contributions to international organizations such as CERN and ESRO.

Turning now to organizational matters, similar chief scientist and chief executive level posts will be established in all the customer departments, in order to implement the customer/contractor policy. In general the approach to providing staff with rewarding careers, particularly those scientists and technologists with managerial ambitions, seems forward looking. However, those who have looked especially for a career in basic research may fear they will not find it under the new arrangements.

Lord Rothschild has refuted the critics who claimed to detect antagonism to the Research Councils and it is fair to say that both reports called for a broadly similar 'Council of Research Councils'. The Government's intention to re-constitute the Council for Scientific Policy to include more effective Departmental representation and to serve as an advisory body between the Department of Education and Science and the Research Councils, should reassure the majority in this respect.

It was pointed out by N.E.C.§ that the 'civil' Research Councils of the D.E.S. have tended to be unjustifiably remote from their 'defence' equivalents, and the new C.S.P. will include senior scientists from Departments with a major interest in the work of the Research Councils, and a representative of the Chief Scientific Adviser to the Government. In this way more effective use should be made of the current spending on R & D in the Ministry of Defence of £330M, in the Department of Trade and Industry of £109M on aerospace, £43M on reactor and nuclear research and £26M on industrial research, and in the Department of Environment of £17M. The suggestion by the Select Committee on Science and Technology for a 'Minister for Research and Development' with his own Vote has been rejected, but the independence of major Departments of State must not prevent greater collaboration on research programmes in the interests of the advancement of science and education.

* Comnd. 4814.
† Comnd. 5046.
‡ 'Changes in Government Science', *The Radio and Electronic Engineer*, **41**, p. 525, December 1971.
§ *National Electronics Review*, **8**, p. 48, March-April 1972.

Contributors to this issue

Dr. K. J. Dean (Fellow 1965, Member 1952, Associate 1946) takes up the appointment of Principal of South East London Technical College on September 1st, as announced in the *Supplement to The Radio and Electronic Engineer* for May 1972, page S.69, where a full note on his career was published. He is currently Chairmen of the Organizing Committee for the Joint Conference on 'Computers—Systems and Technology' to be held in London in October.

Dr. Jacques Gilbert received the B.Eng. degree in engineering physics in 1955 and the M.Eng. degree in 1957 from McGill University, Montreal. He joined the Defence Research Establishment Valcartier (DREV), Quebec, in 1957 and until 1965 he was successively engaged in radar counter-measure work and microwave spectroscopy. While working at DREV he received the Ph.D. degree in physics from Laval University, Quebec, in 1968. Since then he has done research and development work on molecular gas lasers. He is currently Head of the Opto-Electronics section and his research work is concerned with CO_2 lasers and their applications to military technology.

Mr. R. S. King graduated from the University College of Swansea with an honours degree in electrical engineering in 1967. He then joined the Plessey Company as an integrated circuit design engineer and in 1968 moved to the pyroelectric infra-red detector team upon its formation and is currently concerned with simulation and testing equipment of the infra-red system.

Mr. Fernand Rheault received the B.Sc.A. degree in engineering physics in 1964 from Montreal Polytechnic School, and the M.Eng. degree in electrical engineering from McGill University in 1970. He joined the Defence Research Establishment Valcartier (DREV) in 1964, where he was involved in solid-state laser applications. Currently he is mainly working in the field of molecular laser research.

Mr. R. J. Eddington attained his L.R.I.C. at Northampton College of Technology in 1966. Until recently he was engaged in the investigation of epitaxial growth of lead-tin telluride. He is presently studying materials aspects of pyroelectric phenomena.

Mr. Jean-Louis Lachambre attended the Polytechnic School of Montreal where he received his B.Sc.A. degree in 1965 and his M.Sc.A. degree in physics in 1967. He then joined the Defence Research Establishment Valcartier (DREV) where he was initially involved in the development of infra-red detectors. Since 1969 he has been working in the field of molecular gas laser research.

Mr. H. Blackburn (Member 1966, Graduate 1964) joined the Plessey Company's Allen Clark Research Centre in 1958. After a number of years of work in thin films and silicon integrated circuit processing he became responsible for a project on infra-red thermal imaging. He serves on the Institution's Components and Circuits Group Committee and was a member of the Organizing Committee for the Conference on Infra-Red Techniques. He was a joint author of a paper on 'Low-pass active filters' read at the Conference on Applications of Thin Films in 1967 and published in the *Journal* in August 1967.

Mr. H. C. Wright, who is also with the Allen Clark Research Centre was a co-author of a paper published in the July issue of the *Journal*, where a fuller note on his career will be found.

U.D.C. 621.375.826.038.823

Actively Mode-locked Transversely Excited Atmospheric (T.E.A.) CO_2 Laser

J. L. LACHAMBRE, M.Sc.A., P.Eng.,*

F. RHEAULT, M.Eng.*

and

J. GILBERT, Ph.D., P.Eng.*

Based on a paper presented at the I.E.R.E. Conference on Infra-red Techniques held in Reading from 21st to 23rd September 1971.

SUMMARY

A mode-locked CO_2 laser with transverse pulse pumping has been developed which employs a Ge ultrasonic diffraction cell as an active loss modulator. This paper describes the initial stage of an effort to exploit the broad bandwidth (~ 5 GHz) of the CO_2 laser transition and the high concentration of active gas at atmospheric pressure for generating ultra-short infra-red pulses at 10·6 μm wavelength. With the laser system presently described, output pulses with typical durations of about 1 ns and peak powers in the multi-megawatt range have been obtained for the first time.

* *Defence Research Establishment Valcartier, P.O. Box 880, Courcelette, P.Q., Canada.*

1. Introduction

With the development of the transversely excited atmospheric (t.e.a.) laser there has been rising interest in the generation of short powerful pulses at 10·6 μm.[1–4] The high concentration of active gas and the extremely large amplification bandwidth available at atmospheric pressure make the t.e.a. laser potentially capable of producing sub-nanosecond pulses with several megawatts of peak power. A first successful attempt to actively mode-lock the t.e.a. CO_2 laser was reported recently by Wood *et al.*[4] using an intra-cavity acoustic loss modulator. So far this is the only atmospheric laser system described in the literature as working in the forced mode-locked regime. The technique employed has been fully exploited in the visible spectrum and consists in synchronizing the phases of the oscillating modes of the laser cavity by amplitude-modulating the laser fields at a frequency close to the axial intermode spacing $c/2L$ where c is the velocity of light and L is the optical mirror separation. In this manner, the modes of the cavity are made to emit as coherent oscillators which interfere constructively to produce a train of narrow pulses spaced $2L/c$ apart. It is evident from Fourier analysis that the duration time of these pulses should be inversely proportional to the number of phased modes spanning the spectral width of the CO_2 transition, and that their peak power should increase in proportion with the number of oscillating modes.

This paper describes the construction, design and performance of a mode-locked t.e.a. CO_2 laser based on a loss modulation scheme similar in principle, but not in detail, to that described by Wood *et al.* A unique feature of the present laser is the combination of a close-to-hemispherical resonator with a discharge tube pulse excited by transverse electrodes of helical geometry at voltages up to 60kV. This arrangement has led to a considerable enhancement in the peak power and energy attained with a single transverse mode operation. Pulse widths around 1 ns at peak powers of 3–5 MW have been measured with instrument-limited resolution. These pulses are believed to be the strongest ones obtained to date from a CO_2 laser. In this mode-locked operation of the laser, the generation occurs in the form of a short pulse train which lasts typically 100–250 ns, as a result of the gain-switched character of the pulsed excitation. The system operates at a repetition rate 1–10 shots per second with an overall output of roughly 0·1 joule per shot.

2. System Design

This section is concerned with the details of the operation and the design of the major components of the mode-locked laser system. A block diagram of the laser and the associated intracavity modulation arrangement to obtain mode-locking is shown in Fig. 1.

2.1. *The Laser*

The discharge cell is constructed of a 150 cm length of acrylic tubing with an internal diameter of 3·5 cm and closed at both ends by NaCl Brewster windows. The electrical discharge is established transversely to the tube axis by a pair of longitudinal point electrodes

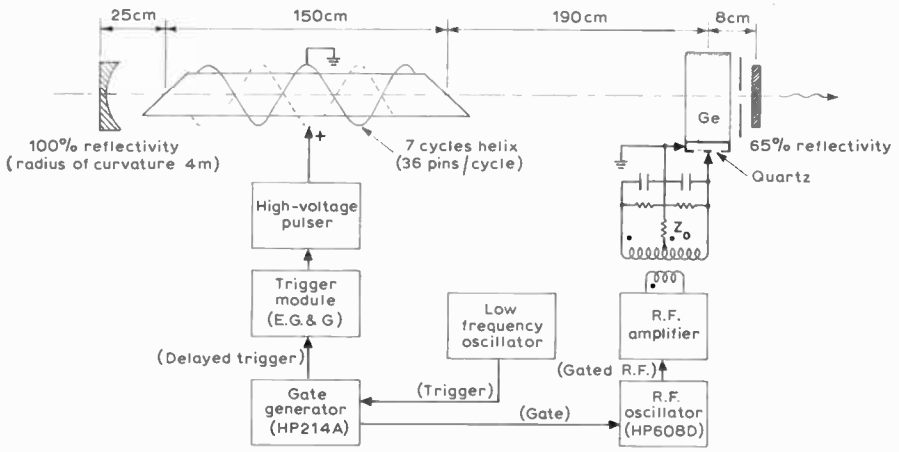

Fig. 1. Block diagram of the complete mode-locked laser system.

arranged as two concentric helices with a gap spacing of 2·5 cm normal to the axis. An array of 1 kΩ ballast resistors spaced 0·5 cm apart and interconnected by short heavy leads forms the positive electrode while a simple array of resistanceless pins is employed as ground electrode. Both electrodes are supported on the insulating acrylic tube by compressing the pins and the resistor leads into individual holes drilled in the tube wall with the vacuum seal being secured by a plastic adhesive.

A three-component mixture of CO_2:N_2:He (1:1:8) flows continuously over the entire length of the laser and is exhausted to the atmosphere at a rate of 4000 cm^3/min by a mechanical pump. This flow-through system allows operation over a wide range of pressures below one atmosphere. A 4 metre curvature concave mirror of 100% reflectivity and a semi-transparent Ge flat (reflectivity 65%) constitute the laser cavity. The reflectivity of the output coupling window was chosen here for maximum laser energy output near atmospheric pressure. The mirror separation is adjusted to provide a near-hemispherical geometry having an axial mode interval of 40 MHz. The mirrors are mounted external to the discharge tube which is positioned as close to the concave mirror as possible. Pulse pumping is effected by discharging a 0·01 μF capacitor through the laser tube with a fast EG & G spark-gap switch. Discharge-current pulses of 2000 A and 0·5 μs full width are supplied to the gas mixture at a repetition rate of 1–10 pulses per second, which is limited mainly by the charging time of the capacitor. With these strong short current pulses, the CO_2 gas is pumped to a high excess population in a time interval which is short compared to the build-up time of the laser field. As a result, the laser emission acquires a Q-switched character, and the energy stored in excess population is converted to a giant pulse 100–250 ns in duration, which occurs roughly 1–2 μs after the current discharge.

2.2. *The Modulator*

In the present laser, the phase synchronization of the axial modes is accomplished by means of an acousto-optic loss modulator. Basically, acousto-optic modulation is a technique in which a phase grating is periodically induced in a crystal cell by generating time-varying deformations in the dielectric material with an acoustic standing wave. The transmitted light beam is thus amplitude-modulated at twice the frequency of the ultrasonic excitation through scattering into the higher diffraction orders. A single crystal of Ge cut in the form of a 1 cm cube was chosen here as an acoustic cell. In order to couple this cell to the electrical circuit, an X-cut quartz crystal resonant at 20 MHz is fixed to one side of the Ge block with a Dow Resin 276-V9. Electrical connexion is made to the quartz electrode by spring clamping the transducer-crystal unit to a chassis-type BNC connector to which the ultrasonic drive is applied. A photograph of this modulator arrangement is shown in Fig. 2. The crystallographic orientation of the Ge block was determined by x-rays. To favour the mode-locked condition corresponding to a single circulating pulse of minimum duration within the cavity, the modulator is spatially isolated from the CO_2 amplifying medium by placing it directly adjacent to the output coupling mirror. The (111) direction is aligned along the polarization vector of the optical beam defined by the orientation of the Brewster windows, while the acoustic wave is launched collinearly with the polarization at right angles to the laser axis. The mount of the crystal has a limiting aperture of 1 cm^2 which is very effective in suppressing the off-axial modes. Anti-reflexion coatings are deposited on the (110) faces to provide a single-pass transmission slightly less than 8% at 10·6 μm. The modulation characteristics of this arrangement were measured with the aid of a stabilized c.w. CO_2 laser and a rapid

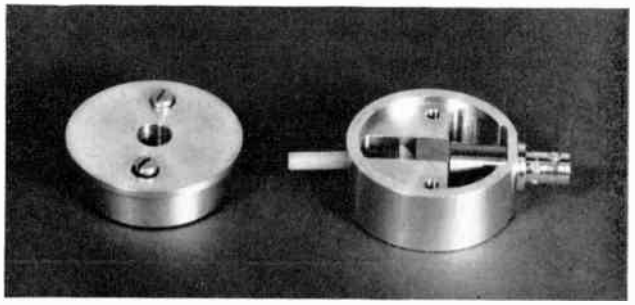

Fig. 2. Acousto-optic modulator assembly.

Hg-Cd-Te detector. It has been estimated that, for a modulator drive smaller than 20 V peak-to-peak (referred to the input of the electrical coupling network), the modulation index varies almost linearly with the acoustic power level. The maximum modulation index attained is 30–40%, but the transmission loss is substantial at these high drive levels. Stable and reproducible modulation characteristics can be achieved on a number of acoustic vibration modes (intermode spacing ~ 250 kHz). However, the modulation efficiency is not identical on these modes, and a selection has to be made for optimum results.

2.3. *Mode-locked Operation*

In order to eliminate the danger of damaging the transducer crystal through high-voltage arcing, and also to minimize the power output requirement from the ultrasonic driver, it was found desirable to operate the modulator in a pulsed regime compatible with the pulsed pumping of the discharge tube. With the modulator design presently adopted, however, the transient build-up of the acoustic field in the crystal cell is exceedingly long compared to the time required for laser excitation and emission. Hence, to achieve a high optical modulation index, the switch-on time of the laser has to be delayed until the acoustic standing wave is fully developed. A basic requirement is to provide the radio frequency power to the modulator in correct phase synchronism with the instant of laser action.

This synchronization scheme is illustrated schematically in Fig. 1. A start pulse supplied by a low-frequency oscillator triggers a pulse generator (Hewlett Packard 214A) which in turn generates a gating waveform together with an adjustable delayed trigger pulse. The latter pulse is fed directly to an EG & G trigger module that fires the spark-gap switch in the high voltage pulser. In this way the discharge-current pulse is retarded with respect to the leading-edge of the gating waveform and can be made to occur at any desired instant within the time span of the gated r.f. pulse. The gate is used to turn on a normally quiescent oscillator (HP 608D) tuned to half the axial mode interval of the laser cavity. This pulse is delivered to the modulator via a tunable r.f. driver and a coupling network. Coupling is effected by a balanced-type L-C circuit in which the crystal and its associated transducer are utilized as one arm of a bridge. This provides an arrangement whereby the acoustic field can be monitored by observing the signal unbalance across the centre-tap termination Z_0. This feature is useful for setting the frequency of the r.f. drive on the centre frequency of the acoustic mode.

The operation of the system is illustrated in Fig. 3. The timing relationship between the gated r.f. signal and synchronizing pulse for the laser excitation is indicated by the waveforms A and C. The gate has a duration of 1 ms and is activated about 800 μs prior to the occurrence of the laser pulse. As can be seen from waveform B, appearing at the bridge termination Z_0 of the coupling network, the transient acoustic response accompanying the abrupt turning on and turning off of the r.f. drive is exponential with a characteristic time on the order of 200 μs. Owing to the small electroacoustic coupling efficiency of the quartz transducer, the acoustic field is forced to grow and decay relatively slowly as compared with the acoustic transit time in the Ge block. An expanded display of laser action showing the sequence of appearance of the giant laser spike and of the discharge trigger pulse is also given by the waveforms D and E. The main difficulties associated with this modulator are: (i) since the electroacoustic coupling of the quartz transducer is inherently small, the high Q value of the mechanical resonance results in an appreciable impedance being offered to the external circuit, thus complicating the matching problem with practical L-C circuits; (ii) because of the high impedance mismatch between the transducer and the external circuit, the r.f. voltage needed to produce a large degree of modulation is undesirably high; finally (iii) since the overall Q of the acoustic resonance is high, the ultrasonic frequency must be very stable to maintain the resonance condition necessary for reproducible operation over long periods of time.

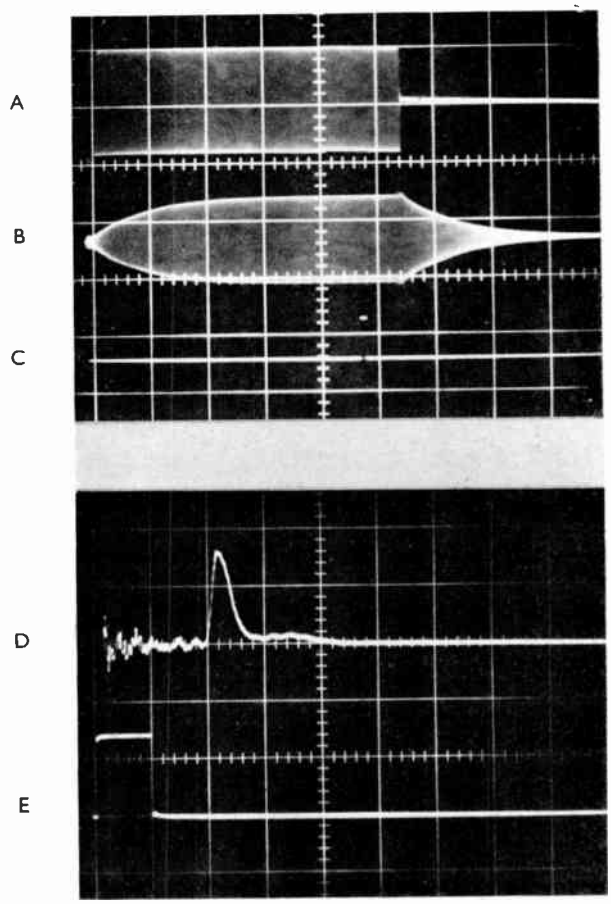

Fig. 3. Waveforms illustrating the operation of the mode-locked laser system. (A) Pulse output of the gated r.f. oscillator; (B) growth and decay of the acoustic field in the Ge cell, observed at the bridge termination of the transducer coupling network; (C)-(E) delayed trigger for initiating the discharge-current pulse; (D) trace of the entire gain-switched laser pulse (mode-locked structure is washed out by the slow response of the oscilloscope). For curves A, B and C, time-base: 200 μs/cm; for curves D and E, time base: 1 μs/cm.

3. Performance and Discussion

3.1. *Laser Output Characteristics*

The experimental dependence of the gain-switched pulse energy upon the total gas pressure for different mixtures of CO_2-N_2-He is plotted in Fig. 4. These measurements were performed using a calibrated pyroelectric detector[5] with the modulator inserted in the cavity but without the r.f. drive being applied. The characteristic feature of these curves is the presence of an optimum total pressure for a given gas mixture. It is seen that this optimum pressure increases as the He concentration is raised while the corresponding energy maxima are broader and less intense. A strong correspondence was noticed between the drop in pulse energy at high pressure and the tendency for the individual discharges to change from the abnormal glow to the arc regime. This tendency could be somewhat diminished at the expense of a decrease in laser generation by lowering the energy storage capacity of the high voltage pulser.

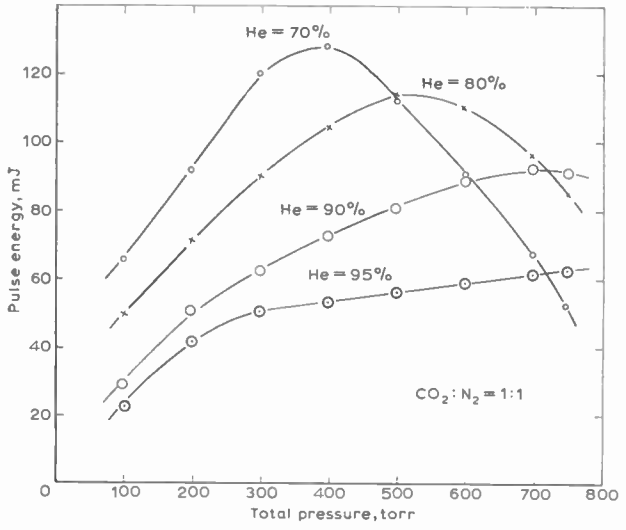

Fig. 4. Experimental dependence of pulse energy on total pressure at different He concentrations for fixed proportions of CO_2-N_2.

Apart from an overall enhancement in energy output, the general pattern of these curves is relatively unaffected when the laser is allowed to operate in a multi-mode regime by taking the modulator outside the cavity. The optimum results in the mode-locked operation are obtained with a CO_2-N_2 pressure ratio of about 1:1 at He concentrations slightly higher than 80%. The loss in output energy incurred by operating at a reduced CO_2-N_2 concentration is largely compensated by a better energy reproducibility from one shot to the next. This appears to be connected with the stability of the discharge, and is considered to arise from the high thermal conductivity of He and its consequent cooling effect on the discharge.

The spectral content of the laser radiation was analysed using a grating spectrometer. All the wavelengths seen in oscillation were identified as belonging to the P-branch of the 001-100 vibrational band near 10·6 μm. Over the pressure range 100-760 torr the laser oscillations are restricted mainly to a single rotational line which under the best alignment conditions is the P(18) transition. This is due to the fact that near atmospheric pressure, the characteristic time for thermalizing the rotational populations of the CO_2 molecules is shorter than the time over which the laser emission takes place. This time which corresponds to the mean time between collisions is given by the reciprocal of the laser linewidth and is expected to be of the order of 0·1 ns. Below 100 torr, however, more than one line may be found to oscillate simultaneously with some competition among them. The switching-on of the modulator drive appears to exert very little influence on the spectral content of the laser output. The characteristics of the output beam were also checked by scanning the far-field pattern with a pinhole and a detector. These measurements showed a near-Gaussian mode structure with a divergence less than 3 mrad. Higher energies can be obtained by operating the cavity as near as possible to the concentric geometry. Under these conditions surface damages are consistently produced by optical breakdown on both the modulator crystal and the output coupling window.

3.2. *Active Mode-locking*

The detailed mode-locked structure of the giant laser spike was monitored by a calibrated photon drag detector[6] and displayed by a real-time oscilloscope (HP 183A). The combined rise-time of this detection system is limited primarily by the resolution of the oscilloscope which is a little less than 1·5 ns. The slow repetition rate of the high-voltage pulser precluded the possibility of using faster sampling techniques.

Figure 5(a) shows the oscilloscope trace of a typical gain-switched pulse observed at an operating pressure of 700 torr when the modulator was passively present in the laser cavity. Despite the absence of modulation the giant laser pulse has a spiky character with periodicity at even and odd multiples of the axial mode spacing. Owing to the large spectral width of the laser line, several axial modes are inevitably excited, and their mutual interaction through the saturation non-linearity of the amplifying medium gives rise to intensity fluctuations at the cavity round-trip time interval $2L/c$. This kind of self-pulsing which takes place spontaneously in any multi-mode laser is random and unpredictable, but occasionally can produce very intense nanosecond pulses. Figure 5(b) shows a train of narrow pulses emitted under conditions similar to the above but with forced mode-locking. In contrast with the multi-pulsing behaviour of spontaneous self-locking, the active mode-locked regime is characterized by clean pulsations at $2L/c$ intervals indicating the presence of a single pulse within the cavity. With optimum modulator drive, corresponding to a modulation depth of about 20%, this locking situation is very stable from pulse to pulse and is found to persist throughout the laser emission. The shape of this mode-locked pulse train is consistently reproducible over the full pressure range of the laser with little jitter in starting time. In the low pressure region, when the

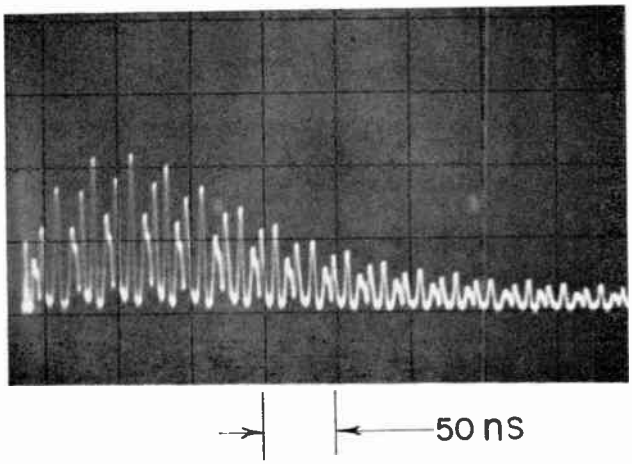

(a)

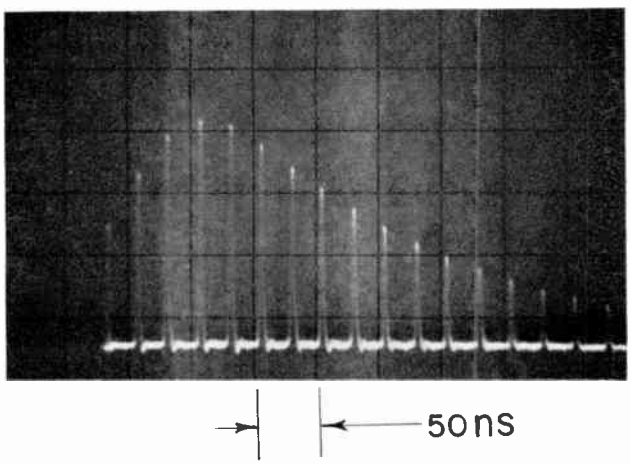

(b)

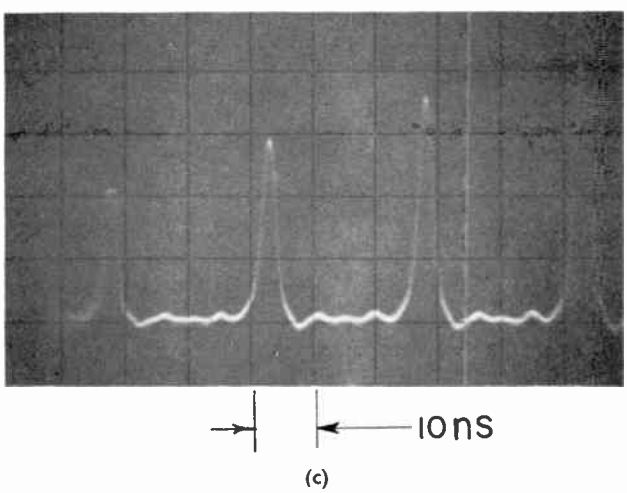

(c)

Fig. 5. Oscilloscope traces showing the detailed structure of the mode-locked pulse trains: (a) without modulation (spontaneous mode-locking); (b)-(c) with modulation (active mode-locking).

modulator is turned on, there is a pronounced enhancement of peak power, by a factor 3 to 5, over the average fluctuations of the spontaneous locking state. At atmospheric pressure, however, the most powerful self-locked pulses are as intense as the fully mode-locked pulses. The similarity of peak power in these two different locking situations is noteworthy. This may be taken as evidence that the non-linearity of the medium together with the huge atmospheric bandwidth of the CO_2 gas is capable of phase synchronizing as many modes as the loss modulation mechanism alone. Obviously the strong competition existing between these two pulse compression mechanisms renders any interpretation of the mode-locking behaviour of the laser extremely difficult. In Fig. 5(c) a few of the narrower pulses observed are illustrated with a faster sweep speed. The indicated peak power of these pulses is 3–5 MW and their width measured at half height is 3 ns which is roughly the limit of resolution of the display system. The uncertainty in display leads here to an underestimation of the true width and peak power of these pulses.

Kuizenga and Siegman[7] have considered theoretically the formation of ultra-short light pulses in an internally loss-modulated laser having a collision-broadened amplification bandwidth. From this analysis a limiting duration of the mode-locked pulses is given by the expression

$$\tau_p = \sqrt{\frac{\sqrt{2(\ln 2)}}{\pi^2}} \left(\frac{g_0}{\delta_l}\right)^{\frac{1}{2}} \left(\frac{L}{c\Delta\nu}\right)^{\frac{1}{2}}$$

where g_0 is the single-pass saturated power gain ($\simeq$ cavity losses), δ_l the modulation index, and $\Delta\nu$ the full spectral width of the laser line. An estimate of $\Delta\nu$ for a typical CO_2-N_2-He mixture (10:10:80) can be made from the self-broadening data of Rosetti and Barchewitz[8] and of Patty *et al.*[9] This leads to the value $\Delta\nu \simeq 5$ GHz at atmospheric pressure. Using this, together with the parameter values appropriate to the laser, the minimum pulse duration is calculated to be $\tau_p \simeq 0{\cdot}8$ ns, in reasonable agreement with the present observations. In an attempt to obtain an estimate of the limiting duration of these pulses, a test was made to check the dependence $\tau_p \propto (\Delta\nu)^{-\frac{1}{2}}$. By taking the total pressure as a measure of $\Delta\nu$ it was found that τ_p decreases roughly as $(\text{pressure})^{-\frac{1}{2}}$ over the range 10–200 torr. Above 200 torr the pulse width measurement becomes instrument-limited and the pressure has negligible effect on τ_p. An extrapolation, up to one atmosphere, of the low pressure dependency suggests that the true pulse width must lie in the subnanosecond range. A similar attempt was also made at testing the dependence $\tau_p \propto (\delta_l)^{-\frac{1}{2}}$, but this proved to be extremely difficult as a consistent and reproducible pattern of data could not be obtained. An important complication is the change in modulator transmission loss accompanying the change in r.f. drive level. At high modulation indices, this loss tends to quench the laser oscillations, thus severely restricting the permissible range of measurements. About all one can say is that at low modulation drive there is a definite evidence of pulse compression with increasing modulation depths. Clearly though, because of several uncontrollable factors connected with the high pressure multiple discharge in the laser (such as the thermally-induced cavity distortions and the spatial non-uniformity of pumping), the conclusions drawn from such experiments must be regarded as tentative.

It may be significant to note that forced mode-locking can be achieved with as little as 15% modulation at atmospheric pressure, which is less than the value quoted by Wood *et al.*[4] The modulation thereshold for mode-locking appears to be lower the lower the pressure. As a final point, we remark that, due to the small width ($\simeq 200$ ns) of the gain-switched pulse train, the spectral contribution of the finite pulse train to the oscillating modes extends over several megahertz. As a result, the mode-locking is not critically dependent on the cavity length or on the r.f. drive frequency. Reliable mode-locking with negligible effects on the pulse duration is obtained over a range of variation in cavity length of several centimetres.

4. Conclusion

It has been demonstrated that, in the mode-locked regime of operation, a t.e.a. laser can generate extremely short pulses at peak powers which were previously unattainable with CO_2 lasers. An extrapolation of the experimental pulse width dependence on pressure, based on theoretical predictions, provides some evidence that the duration of these pulses lies in the subnanosecond region. However, an accurate and reliable method of measuring ultra-short pulses at 10·6 μm is lacking at the present time, and the question of peak power and pulse duration raised in the present work must be considered as incompletely settled. It is expected that these pulses will find extensive applications in research areas such as plasma physics and non-linear optics and in the fields of radar and optical ranging.

5. Acknowledgments

The authors are indebted to Mr. R. Morin for assistance with the measurements and the construction of the laser, and to Dr. R. Fortin for numerous discussions. Thanks are also due to Mrs. S. O'Brien for help in the preparation of this manuscript.

6. References

1. Lyon, D. L., George, E. V. and Haus, H. A., 'Observations of spontaneous mode-locking in a high-pressure CO_2 laser', *Appl. Phys. Letters*, **17**, pp. 474–6, December 1970.
2. Gilbert, J. and Lachambre, J. L., 'Self-locking of modes in a high-pressure CO_2 laser with transverse pulse excitation', *Appl. Phys. Letters*, **18**, pp. 187–9, March 1971.
3. Smith, D. C. and Berger, P. J., 'Mode-locking of an atmospheric pressure cross-excited electrically pulsed CO_2 laser', *I.E.E.E. J. Quantum Electronics*, QE-7, pp. 172–4, April 1971.
4. Wood, O. R., Abrams, R. L. and Bridges, T. J., 'Mode-locking of a transversely excited atmospheric pressure CO_2 laser', *Appl. Phys. Letters*, **17**, pp. 376–8, November 1970.
5. Lachambre, J. L., 'A pyroelectric energy meter', *Rev. Sci. Instrum.*, **42**, pp. 74–7, January 1971.
6. Gibson, A. F., Kimmitt, M. F. and Walker, A. C., 'Photon drag in germanium', *Appl. Phys. Letters*, **17**, pp. 75–7, July 1970.
7. Kuizenga, D. J. and Siegman, A. E., 'F.m. and a.m. mode-locking of the homogeneous laser—Part 1: Theory', *I.E.E.E. J. Quantum Electronics*, QE-6, pp. 694–708, November 1970.
8. Rosetti, C. and Barchewitz, P., 'Détermination du moment de transition vibrationnel et des largeurs des raies de vibration-rotation de la transition $\nu_3 \rightarrow \nu_1$ de CO_2,' *C.R. Acad. Sci., Paris*, 262B, pp. 1199–1202, May 1966.
9. Patty, R. R., Manring, E. R. and Gardner, J. A., 'Determination of self-broadening coefficients of CO_2 using CO_2 laser radiation at 10·6 μ,' *Appl. Optics*, **7**, pp. 2241–5, November 1968.

Manuscript first received by the Institution on 14th May 1971 and in revised form on 15th February 1972. (Paper No. 1464/CC140.)

U.D.C. 681.327.67

The Organization of Some Solid-State Stores

K. J. DEAN, M.Sc., Ph.D., F.Inst.P., C.Eng., F.I.E.E., F.I.E.R.E.*

SUMMARY

A basic solid-state storage array is proposed which is capable of fast read- and write-times. Special cases of this array are developed, one of which is analogous to a disk store and the other to a toroid on which the data paths can be either circular or helical. This represents a new concept: that of a cellular array without boundary cells. The characteristics of these stores and those of other conventional forms of storage are compared.

* *Formerly Twickenham College of Technology; Principal-designate, South East London Technical College, Lewisham Way, London SE4 1UT.*

1. Introduction

The design of a computer store must inevitably be a compromise amongst a number of factors which are seldom compatible. The weighting given to these factors is dictated by the precise use of the store as part of a computing system. They include the access time (which may be divided into read- and write-times), the size of the store, its method of organization and the target cost per bit of storage. This cost is often a factor which is dependent on the overall size of the store. For example, the cost per bit for a magnetic disk store falls as the size of the store increases.

The correct choice of technology with which to solve a particular storage problem depends on the state of development of the technologies which are available.[1,2] These include ferrite cores, magnetic disks and semiconductors[3,4] although considerable effort has been devoted to other technologies, for example plated wires and thin films,[5,6] optical storage,[7] and ovonic switches.[8] Recently a growing interest has been shown in the design of solid-state stores,[9] particularly as our understanding of metal oxide semiconductor (m.o.s.) technology has improved.[10]

It is intended here to examine the organization of some semiconductor stores. Such stores have, so far, been limited by size and flexibility, magnetic storage systems being preferred where one wished to build up large libraries of data for up-dating and reference over extended periods of time. It is not suggested that solid-state stores can compete with magnetic disk stores as large back-up files but it is contended that there is a need for larger semiconductor stores than are available at present. The nature of this investigation is that of a feasibility study for this type of store. As such it is inevitable that the ideas which are put forward will be related to specific devices and their characteristics, and hedged around with references to 'state-of-the-art' in m.o.s. and bipolar technology. The cost figures which are relevant here showed considerable changes in the last few years but it may be expected, in bipolar technology at least, that the rate of change will decrease in future. It is left to the discerning reader to interpret these figures as trends rather than absolute values at some specific date. These trends are, of course, germane to the arguments which will now be put forward.

The first m.o.s. random access memories were introduced in U.S.A. in 1965, and in 1967 dynamic m.o.s. shift registers became available.[11] However, surface problems with m.o.s. slices have only been solved (by nitride passivation) since about 1968 and before this catastrophic failure of chips was quite common.

Figures 1 and 2 give some idea of current costs and areas of application for the various technologies and show that for some sizes of store with certain access times there are areas of overlap where two technologies are in competition. One of the effects of research and development is that the locations of these areas of overlap are constantly changing. Recently larger m.o.s. stores on single chips have been put on the market, (typically up to 4 kilobits), some of the characteristics of which are competitive with ferrite-core stores and

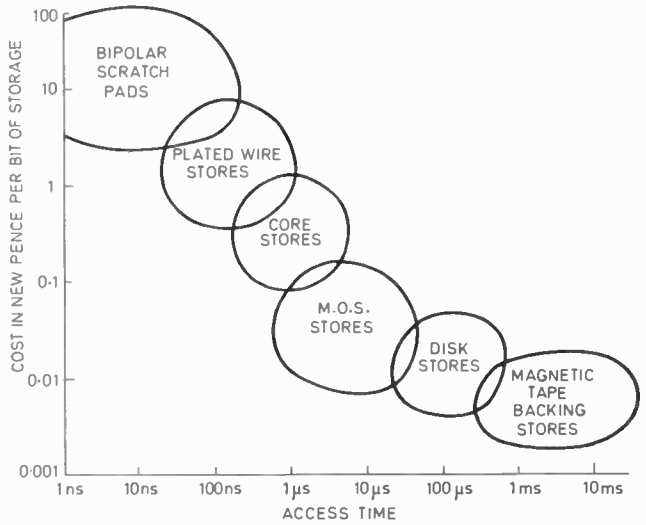

Fig. 1. Comparison of costs of various types of storage. (Note: The cost of tape stores falls as the size of the store increases, whereas that of m.o.s. stores is substantially independent of store size.)

plated-wire stores.[12] It is proposed in this paper to discuss some solid-state stores which may be competitive with small disk or core stores. Although these could be implemented in any of the solid-state technologies, the aim of this paper is to describe the design of a store which has the advantage of the low cost of m.o.s. devices coupled with the high speed which is characteristic of bipolar stores.

2. Basic Storage Circuit and Array

Figure 3 shows a solid-state storage circuit which may be regarded as a basic or generalized circuit from which other simpler or less versatile circuits may be derived. This circuit consists of a D-type flip-flop together with two AND gates. The input gate is controlled by the 'write address' line which also triggers the flip-flop. The output AND gate, which takes data to the 'read data' line must in this design be capable of wired-OR connexion. The cellular representation[13] of the circuit on the right in Fig. 3 can be used when it is not desired to show the circuit detail, but rather to illustrate a storage system with a number of locations as in Fig. 4.

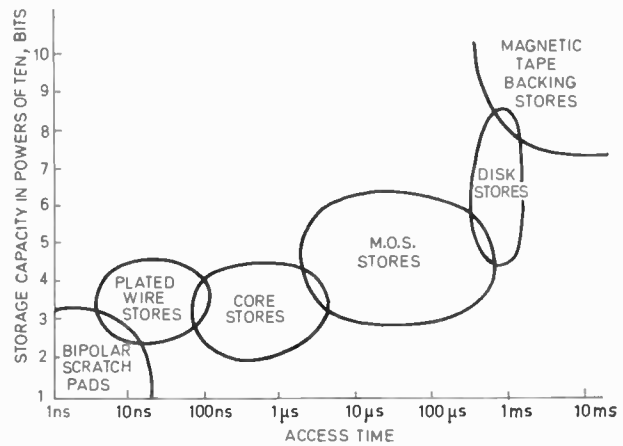

Fig. 2. Typical storage capacities of various types of store.

The organization of the somewhat trivial memory array shown as an example in Fig. 4 is that a 3-bit data word at the inputs labelled WD can be written into column 1 by a pulse on the line labelled WA 1, or into columns 2 or 3 by a pulse on line WA 2 or WA 3 respectively. Similarly these words can be read at the 'read data' outputs RD by a '1' on the appropriate RA (read address) line. A system like this has potentially short read- and write-times determined principally by the time taken to energize the correct address line and by the speed of the solid-state circuitry which is used.[14] It will be observed that unlike cellular arithmetic arrays[15,16] each cell is isolated except for power supply and control lines, from its neighbours, for there is no direct connexion from the output of any cell to any input of a neighbouring cell.

It may be contended that Fig. 4 does not represent a completely generalized store since access is only available to and from a complete column of the store at any one time. This type of arrangement is typical of bipolar scratchpad memories. If access is required to any specified bit or to bit-strings of variable length then

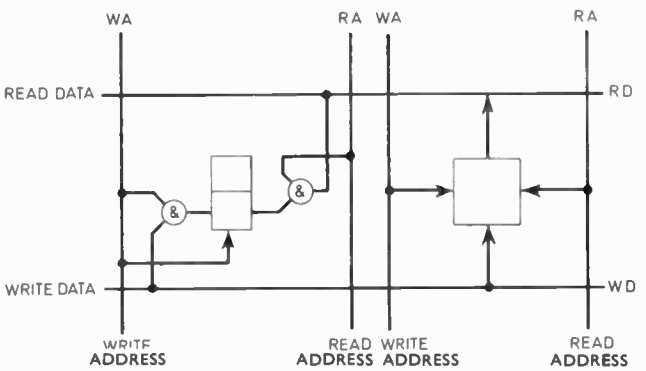

Fig. 3. Basic memory circuit showing the basic element as consisting of logic elements at left and cellular representation of circuit at right.

separate read- and write-lines would be needed for each cell or some coding arrangement must be introduced so that any specified cell can be accessed. Such an arrangement will not be considered further here.

3. Queueing Arrays

The general cell of Fig. 3 may well be simplified if one is prepared to sacrifice some of its versatility in order to achieve a reduction in the cost per bit of storage. Connexion between neighbouring cells for the transmission of data from cell to cell may, for example, be considered. However this changes the character of the array so that it becomes in effect a queue. For example one may be restricted to writing only into column 1 in Fig. 4. Then in order to pass data on to some later column in the array one must rely upon shifting the data through the array. Thus to access a particular location in the array, the operation of the store becomes analogous to that of a multi-bit shift register.

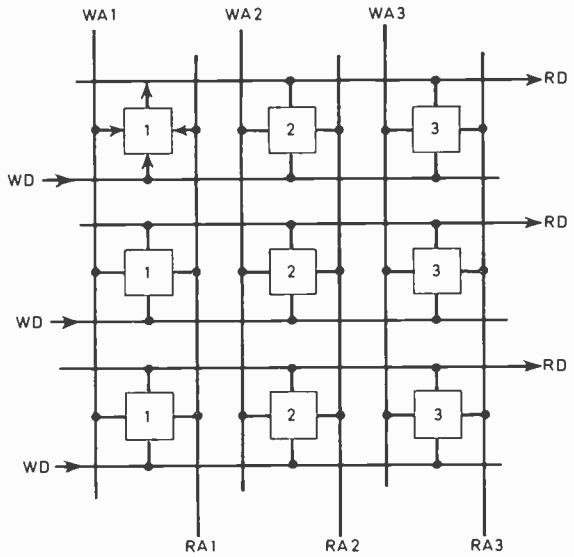

Fig. 4. A section of a solid-state memory array using the cells of Fig. 3. This section shows the organization of three 3-bit words.

4. Dynamic M.O.S. Storage

The cost of a solid-state store depends on a number of factors, including the number of interconnexions between chips. In particular it is directly proportional to the area of silicon which is used. Thus any development which reduces this area is of great importance, and anything which increases it makes the solid-state store less viable.

A basic bistable element consists of four transistors and has a restricted mode of address only. A typical D-type flip-flop using m.o.s. transistors consists of eight interconnected devices and on a single chip occupies a silicon area of about 35 square mils (22 750 μm^2). These are both examples of static storage. Dynamic stages which operate on stored charge must either be refreshed at about 2 ms intervals or operate on a recirculating basis. These cells occupy only 12 square mils (7800 μm^2) of silicon. It seems at the present time that only a low-voltage threshold dynamic m.o.s. system offers low cost with short access time. Recently, improvements[17] have resulted in dynamic stages which consist of a single transistor and a capacitor so that the surface area is reduced to about 6 square mils (3900 μm^2) thus doubling the size of a practical m.o.s. random access memory on a chip and reducing the cost per bit for such stores to an estimated 0·05 p, reducing to 0·01 p per bit when design costs are amortized over large quantities.

The speed of dynamic m.o.s. elements has risen from less than 1 MHz when they were first introduced to over 2 MHz with the probability of 5 MHz clock rates within 2 years. The clock generators are typically 2- or 3-phase systems. Bipolar register stages commonly operate at 25 MHz and 100 MHz operation can be confidently predicted. In this paper comparisons will be made on the conservative figures of 2 MHz and 20 MHz respectively. This 1 : 10 speed ratio is thus likely to improve to 1 : 20 in the near future.

Thus whilst Fig. 1 shows that a dynamic m.o.s. store is cheaper than if bipolar units had been used, the relatively slow speed of m.o.s. circuits results in a low progression rate of data within the store. This is important if the memory is sampled from a static address position or when data must be inserted into a static location, as will be the case when a number of parallel data tracks are being continuously recirculated past a specific read-out. This latter type of memory is analogous to a disk but its write-time compares unfavourably with that of a magnetic disk store. For example, if there are 80 tracks and the storage capacity is 1 megabyte, then 10^5 stages will be needed and the recirculating time (i.e. the maximum write-time) will be 50 ms on the basis of a 2 MHz clock rate, whereas a magnetic disk of similar capacity will have a write-time of about 5 ms. However, this long write-time could have been reduced if there had been any more tracks for the same size of store, although this might have introduced new organizational problems.

A further consideration is that using the cells which have been proposed in Fig. 5 in a 1 megabyte store, the read-time cannot be as short as it might have been for smaller stores, since the original cell design was based on the use of wired-OR connexions at the 'read' output of each cell. It is not reasonable to suppose that 'near-immediate' access is still practicable with such large numbers of locations in the memory connected to a wired-OR output as was implied in the figures quoted. Hence one cannot expect to assess any one of, say, one million words in this way. Instead it is more usual to write, say, an 8-bit word into a byte of eight consecutive locations on a single track. One can then arrange to access the whole of this track by selecting the appropriate 'read address' line and so transferring all the data it carries on to a single track. There is clearly some advantage if this is a bipolar track capable of high-speed operation. Then, by virtue of its higher speed, the desired data can be quickly moved round the disk and read from the track. This is analogous to a high-speed rim on a disk. Data can be written on to the rim and then moved rapidly round the disk at a higher speed than the disk itself 'rotates'. Using bipolar clock rates one order higher than m.o.s. clock rates, a significant speed saving can be expected from this combined m.o.s.-bipolar system. Also, if the percentage of bipolar circuitry is small the cost will not be significantly different from that of an m.o.s. store.

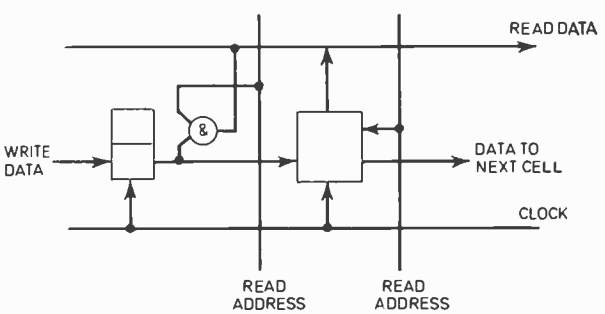

Fig. 5. The basic cell of a queueing array consists only of a D-type flip-flop and an AND gate. The cellular representation of the memory element is shown at the right in the figure.

5. Design Parameters for a Disk Store

Consider a memory of k bits, arranged in m tracks, each of which has n stages, and with an additional rim of n stages of bipolar gates. The m tracks can be accessed by an m-stage register, also of bipolar gates. Let the clock rate of the bipolar cells be x MHz.

$$\text{Storage capacity, } k = m.n \qquad \text{.....(1)}$$

$$\text{Percentage of bipolar logic} = \frac{m+n}{mn+m+n} \times 100 \qquad \text{.....(2)}$$

$$\text{Read-time, } t = \frac{m+n}{x} \qquad \text{.....(3)}$$

$$= \frac{1}{x}(m+k/m) \qquad \text{from eqns. (1) and (3)}$$

$$\text{Hence, } \frac{dt}{dm} = \frac{1}{x}(1-k/m^2)$$

$$= 0, \text{ when } k = m^2$$

$$\text{Hence } m = n \text{ for minimum read-time} \qquad \text{.....(4)}$$

From equation (2) the percentage of bipolar logic (when $k = m^2$)

$$= \frac{200}{m+2}$$

$$\simeq \frac{200}{m} \text{ if } m \gg 2 \qquad \text{.....(5)}$$

From equations (4) and (5) it will be seen that the optimum solid state disk store has m tracks of m elements for minimum read-time, and under these conditions the percentage of bipolar logic is approximately $200/m$. Hence using the previous example of one million bytes we have for a bipolar clock rate of 20 MHz,

storage, k	$= 8 \times 10^6$ bits
no. of tracks, m	$= 2800$
read-time, t	$= 280$ μs
write-time, T	$= 1{\cdot}4$ ms
percentage bipolar logic	$= 0{\cdot}07$ per cent.

If it is assumed that the cost of storage is 0·1 p per bit for m.o.s. circuits and 1·0 p per bit for bipolar circuits, the cost of the store would be £8056. Comparisons of costs and access times for other types of storage are shown in Table 1.

Table 1

Comparison of characteristics for 8-megabit stores

	solid state disk	magnetic disk	core store
read-time	280 μs	700 μs	100 ns
write-time	1·4 ms	700 μs	100 ns
cost	£8056	£4000	£18 000

6. Further Considerations

There are a number of points worth considering in the design of a solid-state store which affect its competitive position with regard to other stores. The percentage of bipolar logic in this design is so small that it has a negligible effect on the cost of storage. It is only worth considering store designs using more bipolar logic if a worthwhile increase in speed could be obtained through using it. For example, had 1% of bipolar logic been used (i.e. an increase of 14 times) the cost would have been £8800, an increase of slightly over 9%. Then using 14 rims of bipolar logic the read-time would be only 150 μs, a reduction of about 47%.

The type of circuit proposed is a dynamic two-state device similar to that shown in Fig. 6. Like most solid-state stores it is volatile, in that stored data are lost on power supply failure. However, this problem can be minimized to some extent by floating its power supplies across a battery. There are cases, however, where such an arrangement would not be reasonable, for example with airborne equipment. Alternatively devices with an oxide-nitride sandwich gate (m.n.o.s. elements) retain charge under these conditions for considerable lengths of time.[18] Although m.n.o.s. gates are only in the laboratory stage of development at the present time it seems reasonable to suppose that this drawback of solid-state stores will soon be overcome. In Fig. 6 the m.o.s. dynamic stores are controlled by a two-phase clock, and in this example, data are only extracted from alternate phases. The half-clock-period delay which this involves, typically 250 ns, is negligible compared with other delays but it halves the number of additional gates required so that, on average, only one additional gate is needed per stage, thus increasing the cost per bit by at most only 33%. Alternatively if a single element transistor-capacitor stage is used as the basis of a memory cell there is a likely saving of about 33% over the conventional 3-transistor stage.

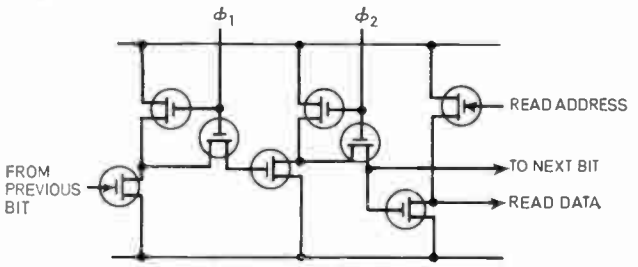

Fig. 6. Two-phase dynamic m.o.s. stages giving two bits of storage with a read-out facility from alternate bits.

There is also the problem of accessing one of a large number of tracks. In the dynamic m.o.s. disk system this operation was carried out using a shift register, but with a slightly different type of memory cell the use of this external register can be avoided and accessing very largely carried out by the cells of the array.

7. Toroidal Store

The memory cell shown in Fig. 5 was analogous to that of a shift register element since in the figure data could only be passed between cells in a lateral direction. A

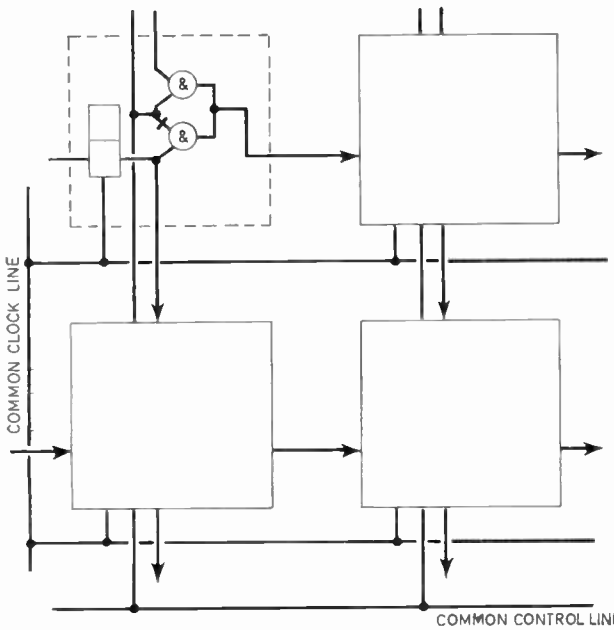

Fig. 7. Two-dimensional cellular memory array showing four cells. The top left-hand cell is seen to consist of a flip-flop, two AND gates and an inverter. The other cells are shown in outline only.

two-dimensional fully cellular array might also have been expected to be able to pass data between cells in a direction at right-angles to that shown, thus making connexions between four neighbour cells. A cell of this kind is shown in Fig. 7. Each cell consists of a D-type flip flop and two AND gates with a wired-OR connexion. Here again a design will be proposed which uses dynamic m.o.s. elements. The control line which is common to all the cells in the array ensures that data either pass laterally across the array or diagonally from top-left in the figure to bottom-right.

Assume first that when the control line is not actuated data pass horizontally in the figure from a cell to its immediate right-hand neighbour through a single AND gate and its wired-OR connexion. When the control line, which is common to all the cells in the array is actuated, data from the flip flop pass from its output connexion to the AND gate in the cell below it and thus to the cell on its right. In each case data pass through a single AND gate. Thus the propagation times are the same for each mode of operation. The complete store must have provision for recirculating in either of these modes and thus the appropriate model for the store is that of a toroid as shown in Fig. 8. Data either pass in circular paths round the toroid or when the control line is actuated the data paths are toroidal helices as shown in parts (a) and (b) of Fig. 8 respectively. Helical data transfer need not take place from every cell and it may be convenient to arrange for this on one phase of a two-phase clock; that is, for alternate cells.

It is contended that this proposal for a toroidal store is an example of a new concept; that of a cellular array which has no boundary cells. It is capable of functioning with every cell connected iteratively to its four neighbours. Thus conceptually it may be of any finite size or infinite. In practice the size of the array will be that of the desired storage capacity and some cells may be specially connected, not only to their neighbours, but to a rim. Also, at the present time a complete store is unlikely to be held on a single chip and so chip size and pin connexions will limit the design of integrated array sections.

The means by which data can be read from the store is, as before, by having a bipolar rim onto which data can be written and which can convey data at a high speed to appropriate reading points. It may be noted that the solid-state disk store originally proposed had a single rim. However, a number of rims might be used with a toroidal store particularly since the previous analysis showed that the percentage of bipolar logic could be increased if there was any speed advantage in doing so. The use of more than one rim means that the length of the spiral path to the rim is reduced, hence reducing the time taken to read data from the store.

8. Design Parameters for a Toroidal Store

Consider a memory of k bits, arranged in m tracks, each of which has n stages and with p rims of n stages of bipolar cells evenly spaced so that m/p is an integer. Let the clock rate of the bipolar cells be x MHz and that of the m.o.s. cells by y MHz. From eqn. (1)

$$\text{storage capacity, } k = mn$$

$$\text{percentage of bipolar logic} = \frac{100p}{(p+m)} \qquad \text{.....(6)}$$

$$\text{read-time, } t = \frac{m}{yp} + \frac{n}{x} \qquad \text{.....(7)}$$

$$= \frac{m}{yp} + \frac{k}{xm} \quad \text{from (1) and (7)}$$

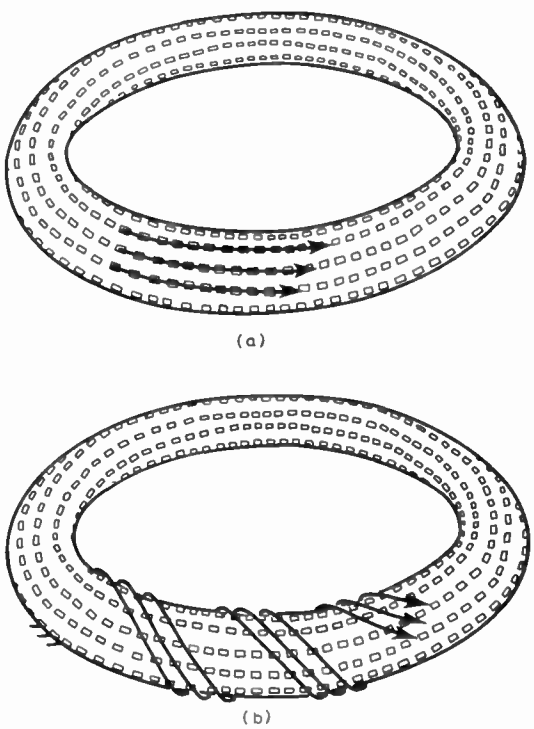

Fig. 8. Toroidal model for a solid-state store showing (a) circular data path, and (b) toroidal helical data path.

$$\text{Hence, } \frac{dt}{dm} = \frac{1}{yp} - \frac{k}{xm^2}$$

$$= 0$$

$$\text{when } m^2 = \frac{kyp}{x} \qquad \text{.....(8)}$$

$$\text{Hence } m = \left(\frac{kyp}{x}\right)^{\frac{1}{2}}$$

for minimum read-time

$$\text{or } m = \frac{ypn}{x} \qquad \text{.....(9)}$$

and from equations (6) and (9) the percentage of bipolar logic, q is given by

$$q = \frac{100x}{x+yn} \qquad \text{.....(10)}$$

$$\text{when } k = \frac{m^2x}{yp}$$

Then

$$q(x+yn) = 100x$$

or

$$qyn \simeq 100x$$

if x is small compared with yn.

Therefore

$$\frac{y}{x} \simeq \frac{100}{qn} \qquad \text{.....(11)}$$

Substituting from equations (1) and (8) in equation (11) leads to

$$\text{number of stages, } m = \frac{kqy}{100x} \qquad \text{.....(12)}$$

$$\text{and number of rims, } p = qm/100 \qquad \text{.....(13)}$$

The write-time was calculated for the solid-state disk store as the time taken for a data location to circle the store completely. On the same basis here, the write-time, $T = n/y$. Then using the example of a 1-megabyte store, the characteristics of a toroidal store with the same device data as for the disk store can be calculated for any given percentage of bipolar logic. Some results are given in Table 2.

9. Comparison between Disk and Toroidal Stores

Comparisons must always depend upon the weight being given to the advantages and drawbacks of the systems being compared. Here a number of attempts at comparison will be made and the reader then left to make his own judgement. It may be contended that any valid comparison of these types of store should be for stores of equal size and equal complexity of organization, that is for an equal number of rims. Thus for a 1 megabyte disk store having 1% bipolar logic in 80 rims the read-time is 150 μs which is slower than the 100 μs previously calculated for a comparable 80-rim toroidal store. The write-time of the disk store would be as low as 100 μs compared with 500 μs for the toroidal store. Hence unless the write-time is of first importance the toroidal store might be thought better.

Table 2

Characteristics of some toroidal stores

bits of store, k	=	8	8	8	$\times 10^6$
no. of tracks, m	=	8	4	1·6	$\times 10^3$
no. of rims, p	=	80	20	4	
no. of stages, n	=	1	2	5	$\times 10^3$
read-time,	=	100	200	450	μs
write-time, T	=	500	1000	2500	μs
percentage bipolar logic	=	1	0·5	0·2	%

Comparison can also be made in terms of the cost of semiconductor material. This can be subdivided into the cost of silicon, which is proportional to surface area, and the cost of interconnexions, that is the number of pins to a convenient section of the store which can be housed on a single chip. Hence if the criteria of comparison are solely those of the size of store and the semiconductor costs, especially the proportion of bipolar circuits, and excludes organizational costs, then the disk store can be shown to be potentially faster. For example a solid-state disk store with 40 000 tracks, each 200 cells long, and which has 200 rims satisfies the condition that it has a capacity of 1 megabyte and 0·5% bipolar circuitry. This array has a read-time of 20 μs and a write-time of 100 μs (using the same criteria as before), both these

Table 3

Pin connexions to some solid-state stores

	general cell (Fig. 3)	queueing cell (Fig. 5)	queueing cell (Fig. 6)	cell of toroidal array (Fig. 7)
no. of data lines	$2n$	$2n$	$3n$	$3n$†
no. of address and control lines	$2n$	$2n$	$n/2$‡	1
no. of power supply lines	2	2	2	2
no. of clock lines	0§	1§	2¶	2¶
total lines	$4n+2$	$4n+3$	$\frac{7}{2}n+4$	$3n+5$
maximum value of n for 32-pin packs	7	7	8	9
no. of pins for a 4·9 kilobit store	282	283	249	215

† Data transfer on alternate phases
‡ Data read-out on alternate phases
§ Assuming single phase clock
¶ 2-phase clock

times being an order better than for a toroidal store. However, the complexity of the associated circuitry would be correspondingly greater.

Turning now to the number of pin connexions to chips of practicable size, Table 3 shows a comparison of the number of connexions to a chip consisting of a section of a store comprising n^2 cells (where n is an even integer) arranged in the form of a square.

Using the data in Table 3 it will be seen that for a 32-pin package the disk store shows a 30% increase and the toroidal store shows a 64% increase in storage capacity over a general store, representing 64 and 81 memory cells respectively. Alternatively, for a 4·9 kilobit store section, the general cell requires 282 pin connexions which is 21% greater than for a disk store and 31% greater than for a toroidal store. Hence on this basis the toroidal store would be regarded as better.

10. References

1. Renwick, W., 'Memories for the next generation of computers', *Electronics and Power*, **18**, pp. 13–16, January 1972.
2. Young, J. F., 'Possibilities of a sinusoidal memory for an extendable cybernetic machine', *The Radio and Electronic Engineer*, **39**, pp. 9–15, January 1970.
3. Lund, T. J., 'Semiconductor memory design', *Microelectronics Quart. J.*, **3**, pp. 42–46, 1971.
4. Hanlon, B. L., 'Design considerations for a high performance 1·1 megabit semiconductor mainframe memory', *ibid.*, **3**, pp. 47–51, 1971.
5. Clegg, W. W. and Pickard, R. M., 'Laminated thin magnetic film memory elements', Proc. Conf. Computer Science and Technology, Manchester, pp. 94–102, 1969 (I.E.E. Conference Publication No. 55).
6. Eilley, E. S., Hughes, J. B. and Richards, N. D., 'Design for an 800 000 bit, 150 nanosecond magnetic thin film store', *ibid.*, pp. 124–9.
7. Scarrott, G. G., 'Optical storage', *The Radio and Electronic Engineer*, **40**, pp. 89–95, August 1970.
8. Walker, P. A., 'Faster computer stores are now economically viable', *Electronic Engineering*, **43**, pp. 32–3, November 1971.
9. Mostyn, R. C., 'The use of m.o.s. transistors in computer circuits', *Marconi Review*, **31**, pp. 189–205, Autumn 1968.
10. Maine, S. G. T., 'Will m.o.s. stimulate a new computer generation?', *Electronic Engineering*, **43**, pp. 27–30, November 1971.
11. English, P., 'Digital applications of m.o.s. integrated circuits', *Marconi Review*, **31**, pp. 171–88, Autumn 1968.
12. Calvert, P. P. A., Gibson, A. T. and Trunley, L. E., 'The next generation—250 nanosecond computer main memories', Proc. Conf. Computer Science and Technology, Manchester, pp. 72–7, 1969 (I.E.E. Conference Publication No. 55).
13. Kautz, W. H., 'Cellular logic-in-memory', *I.E.E.E. Trans. on Computers*, **C-18**, pp. 719–27, August 1969.
14. Linford, J., 'MOS memories for digital systems', *Semiconductors*, pp. 39–44, 1971.
15. Dean, K. J., 'Design for a full multiplier', *Proc. I.E.E.*, **115**, pp. 1592–4, November 1968.
16. Dean, K. J., 'Cellular arrays for binary division', *ibid.* **117**, pp. 917–20, May 1970.
17. Cohen, L., Green, R., Smith, K. and Seely, J. L., 'Single transistor cell makes room for more memory on an m.o.s. chip', *Electronics*, **44**, pp. 69–75, 2nd August 1971.
18. Oakley, R. E., 'MNOS—a new non-volatile store', *Component Technology*, **4**, pp. 17–21, 1970.

Manuscript first received by the Institution on 1st March 1971 and in final form on 10th May 1972. (Paper No. 1465/C141.)

U.D.C. 621.375.826

Factors Affecting the Power Stability of HCN Lasers

D. W. E. FULLER, M.Sc., M.Inst.P.*
and
B. O. BAKER,
B.Sc. (Eng), A.C.G.I., C.Eng., M.I.E.E.†

Based on a paper presented at the I.E.R.E. Conference on Infra-Red Techniques held in Reading on 21st to 23rd September 1971.

SUMMARY

Laser stability must be defined in terms of the appropriate observation period, usually a second, an hour or a day, and the expected changes in the environment during that period. The relative importance of sources of instability of power output has been investigated and related to various designs of the HCN laser. The design of the NPL-GEC laser has been based on this investigation.

* *Division of Electrical Science, National Physical Laboratory, Teddington, Middlesex.*
† *The M-O Valve Co. Ltd., Brook Green Works, London W6 7PE.*

1. Introduction

HCN-stimulated emission was first discovered in a 6m pulsed discharge in 1964[1] and a c.w. laser was first operated in 1966.[2] Since then this source has become widely used as a research tool[3] and many different versions have been designed and constructed at NPL. HCN lasers have been used at the NPL for fundamental measurements like the accurate determination of the speed of light, where a highly monochromatic powerful source of radiation is required, and also for measurements of the transmission characteristics of 337 μm radiation through fog. Other scientists throughout the world have used them for the measurement of plasma parameters for which the particular wavelength is more suitable than those obtained from other lasers. Since the Reading Conference it has been shown that the thermal imaging camera can be used in conjunction with the HCN laser.[10, 11]

The factors affecting the short-term frequency stability have been reported previously.[4] The following discussion deals specifically with power stability but most of the factors considered would also affect the long-term frequency stability. A free-running stable laser based on these considerations has been produced and developed by GEC in collaboration with NPL.

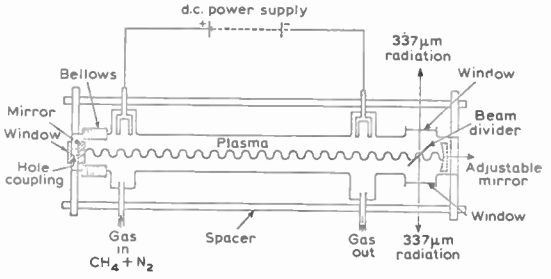

Fig. 1. Basic construction of HCN laser.

The basic construction of an HCN laser is shown in Fig. 1 and the factors affecting its output are shown in Fig. 2. The notation to be used for these factors is given in Fig. 2. The mirrors of the laser illustrated act as a Fabry–Perot resonator and normally only one axial mode is excited at one time for one lasing transition. Both the frequency and magnitude of the output will depend critically on the separation of the cavity mirrors, L, and hence upon the temperatures of the various components of the laser. Long-term frequency stability and resettabilty can be achieved by servo-controlling the cavity length, L, using the near coincident absorption of the difluoroethylene molecule in a passive external gas cell[5]. Long-term power stability can similarly be obtained by monitoring the output power and servo-controlling either the current or the cavity length.[6]

Such methods are necessarily complicated and are justifiable only in highly specialized applications. When designing a laser it is necessary to ascertain the stability required in terms of the detector bandwidth and the observation time and also to estimate the probable fluc-

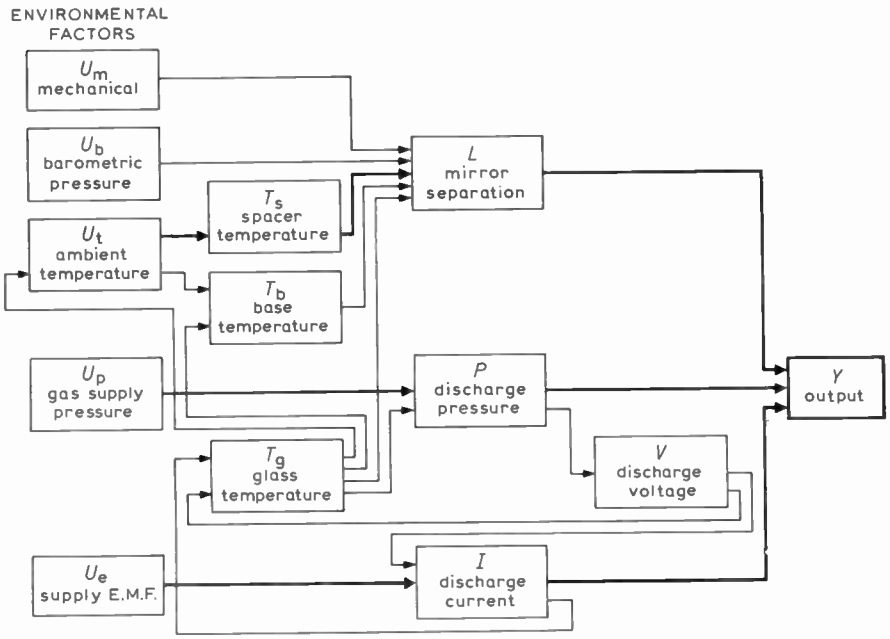

Fig. 2. Factors affecting the power output of an HCN laser.

tuations in the environment. Failure to do this can result in a considerable waste of time either in constructing elaborate lasers or in replication of measurements because of excessive scatter of observations.

2. Definition of Stability

The power stability of the laser is defined as

$$S = \frac{\bar{Y}}{\Delta Y}$$

where $\bar{Y}$ is the mean power received by a detector of given bandwidth;

ΔY is the range of Y observed in a time interval τ, i.e. $\Delta Y = Y_{max} - Y_{min}$.

Considering variations of an input U_q producing changes in the output Y we will write

$$S(U_q) = f(\Delta U_q)$$

For many, but not all, parts of the system it is possible to derive a relationship of the form

$$\frac{1}{S(U_q)} = a\Delta U_q$$

where a is a constant for ΔU_q small.

3. Polymer Deposition

One phenomenon familiar to all users of HCN lasers is the brown deposition of polymeric material on the walls of the discharge tube, on the mirrors and on the beam divider. The power output of the laser reduces progressively with length of operation and this sets the limiting value of stability when the observation period, τ, is of the order of hundreds of hours.

We have found that the rate of reduction of output in the case of a plane parallel laser cavity is determined by the rate of deposition on the walls of the discharge tube but that the confocal cavity is not affected. This provides a direct experimental corroboration of the prediction of Steffen and Kneubuhl[7] that the operation of the plane parallel cavity HCN laser depends upon the reduction of diffraction losses by grazing reflexion from the inner surface of the glass.

If a confocal laser is used then deposition on the beam divider becomes the limiting factor. The slowest rate of decrease of power is obtained in the case of the hole-coupled confocal laser. Deposition does not occur on a surface above 150°C and this is a convenient way of keeping the central section of the discharge tube clean. A hot mirror design is technically feasible should the application justify the expense.

4. Mirror Separation L

Figure 3 shows a typical series of resonances of the powerful 337 μm HCN laser emission. The widths of the resonances will vary depending on whether or not it is operated well above threshold gain. If the laser is initially tuned to resonance and the change in power ΔY and the change in mirror separation ΔL are measured from the

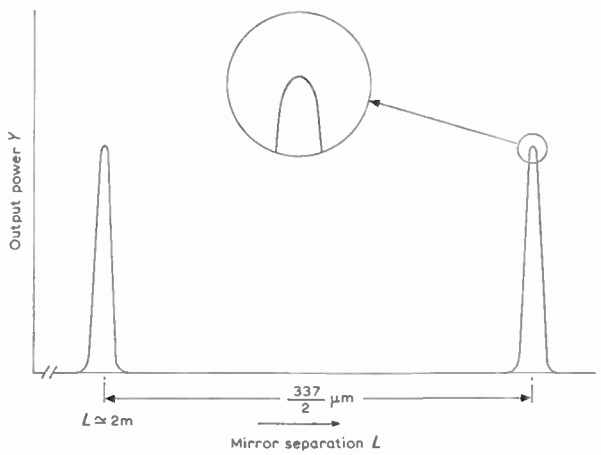

Fig. 3. Consecutive resonances of a single-mode HCN laser.

initial values then

$$\frac{\Delta Y}{Y_{max}} = -a_1(\Delta L)^2 \qquad \text{for small changes}$$

For HCN lasers designed for optimum power output the resonance width is largely determined by the fraction of the laser energy coupled out and it is found that an empirical relation can be used for lasers between 1 and 6 m in length

$$\frac{1}{S(L)} = \frac{\Delta Y}{Y_{max}} = -a_2\left(\frac{\Delta L}{L}\right)^2 \qquad \text{for small changes}$$

where a_2 can be assumed to be 5×10^{10} when designing a laser if measurements taken on a similar laser cavity are not available

i.e. $\frac{\Delta L}{L} = 10^{-6}$ gives $S(L)$ about 20.

It is important to note that reduction of the coupling fraction could lead to a flattening of the resonance curve and a considerable increase in power stability.

The simplest design of laser has mirrors mounted directly on the glass discharge tube. A change of glass temperature ΔT_g of about 0·2 degC will necessitate retuning. If the glass is kept hot enough to prevent polymer deposition then frequent retuning would be required. This design is adequate if the observation time τ is only a few minutes.

Better stability is obtained if mirror spacers having a low coefficient of expansion α_s are used. For a given temperature change of the spacer ΔT_s.

$$\frac{1}{S(T_s)} = a_2(\alpha_s.\Delta T_s)^2 = a_3(\Delta T_s)^2$$

As the square of the expansion coefficient is involved it is important to minimize it. This can be done by a technique comparable to that used in the compensated pendulum[4] or by using silica spacers as in the NPL–GEC laser. By careful thermal isolation of the spacers from the heat generated by the laser it is possible to reduce ΔT_s. to ΔU_t, the change in room temperature. This gives for silica spacers

$$\frac{1}{S(U_t)} = 8 \times 10^{-3}(\Delta U_t)^2$$

It is very desirable to carry out a preliminary survey of the proposed site of a laser. Since the thermal time-constants of the mechanical structural components are measured in minutes it is only necessary to use a simple temperature recorder, together with a source of heat to simulate the laser and ancillary equipment. Measurements taken in one laboratory showed a steady increase of temperature of 1 degC per hour in the morning, random fluctuations of about 0·5 degC in the early afternoon followed by a steady fall at 1 degC per hour until the early hours of the next morning. Under these conditions a laser using silica spacers would be reasonably stable over a period of an hour. Further improvement can be achieved either by thermostatic control of the spacers or of the laboratory whichever is more expedient.

Another factor affecting L is the expansion of the glass discharge tube but this can be reduced considerably by using bellows, or a sliding joint, to take up expansion without placing appreciable tensile forces on the spacers. Similarly the expansion of the base supporting the mirror-spacer assembly will produce mechanical strain and some form of sliding joint or bearing should be incorporated.

An increase in barometric pressure will produce a compression of the mirror spacers but this is usually negligible. A typical change of barometric pressure is 0·1 kN m^{-2} over a one hour interval and for a 100 mm diameter laser the change in compressive force is only 0·8 newtons.

The effects of mechanical disturbances, such as vibration and acoustic noise, are usually unimportant because the laser is heavy and the amplitude of vibration of the mirrors ΔL would have to be relatively large. Observation of frequency changes indicates that $\Delta L/L$ due to vibration is less than 10^{-7} in a normal laboratory environment.

5. Discharge Pressure P

As a very crude approximation we can regard Y as proportional to $(P - P_i)$ where P_i is a constant determined by the current. For small changes in discharge pressure P

$$\frac{1}{S(P)} = \frac{\Delta Y}{Y} = a_4.\frac{\Delta P}{P}$$

where a typical value of a_4 is 5 but because we are considering the fractional changes $\Delta Y/Y$ and $\Delta P/P$ the value of a_4 is increased when working with small values of Y and P.

There is a special case of interest. Consider a laser power supply of e.m.f. U_e with series resistance R. The voltage across the discharge V will increase with pressure P and thus reduce the current I.

Hence

$$\frac{\Delta Y}{Y} = a_4\frac{\Delta P}{P} - \frac{1}{RY}\left(\frac{\partial Y}{\partial I}\right)\left(\frac{\partial V}{\partial P}\right)\Delta P$$

For any given value of R the value of Y will pass through a maximum as P is altered. The fluctuations of pressure will have far less effect on output if the laser is operated in this region.

The gas discharge pressure P is affected by evolution and absorption of gas from the polymer on the discharge tube as its temperature varies. This effect is usually small but can disturb the output for half an hour and give rise to confusing effects.[8] A very early version of the laser was operated sealed-off for tens of hours, the pressure being controlled by appropriate adjustment of the glass temperature. By arranging the resistance of the power supply to be less than the 'resistance' of the discharge it was arranged that a reduction of pressure tended to increase the glass temperature and the laser tended to stabilize its own pressure. Conversely a high series resistance would create an unstable or 'run-away' condition.

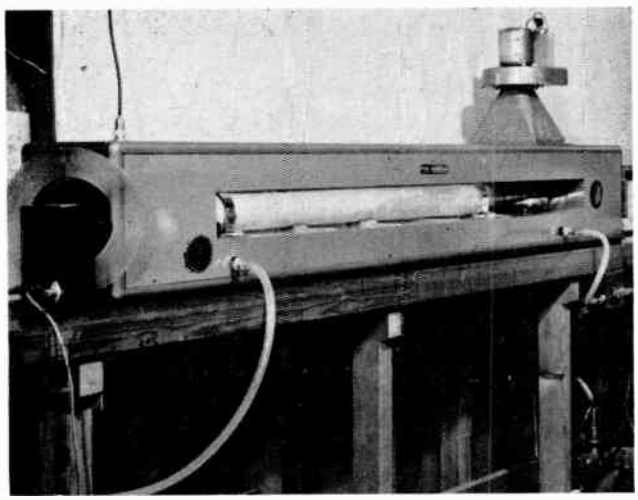

Fig. 4. The NPL-GEC HCN laser.

6. Discharge Current *I*

For a given power output the slope of the curve of power Y against current I does not vary greatly for different pressures. The slope does decrease to some extent at very low pressure but the current required becomes excessive. In theory one could design a laser whose output is independent of current by operating at high currents and low pressures[9] but the power conversion efficiency would be low

$$\frac{1}{S(I)} = \frac{\Delta Y}{Y} = a_5 \frac{\Delta I}{I} \qquad \text{for small fluctuations}$$

where a_5 lies between 2 and 5 for typical laser operating conditions but increases if the laser is operated at low power.

Providing the laser pressure is not varied during the experiment then there is a constant impedance presented to the power supply and an unstabilized power supply will give a sufficiently constant current for many applications. If a Golay cell detector, which has a time-constant of 0·1 second, is used then the presence of 100 Hz ripple on the laser output is unimportant but the use of a fast detector may make a low-ripple stabilized power supply essential.

7. NPL-GEC Laser

This laser (Fig. 4) was produced and developed by GEC in collaboration with NPL, using the principles outlined in the present paper. Mirror spacing is determined with silica spacers whose temperature is carefully controlled. A chart record of power output measured with a Golay cell is shown in Fig. 5, where in a run of 4 hours the standard deviation was 2% of the mean of the power output.

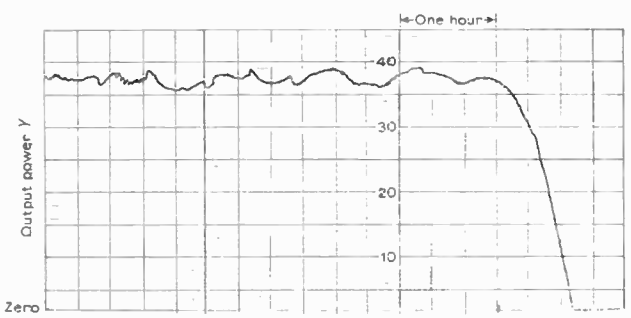

Fig. 5. Stability of laser output. $\bar{Y} = 35{\cdot}7$, $\sigma = 0{\cdot}8$.

8. Conclusions

We may sum up by considering three main groups of measurements.

In the first group the observation period is only a few minutes and the laser current or pressure do not have to be altered as part of the investigation. For these measurements it is sufficient to mount the mirrors directly on the ends of the discharge tube.

In the second group the observation period is about one hour and the measurements are to be made in a laboratory which is not prone to large fluctuations in temperature. A laser using silica spacers, a commercial gas pressure regulator and, if a Golay cell is used, an unstabilized power supply should prove adequate.

In the third group either the observation period is very long, e.g. 24 h, and retuning of the laser is not acceptable, or perhaps the site is exposed to extremes of temperature. In these cases it is essential to monitor the laser output Y and to servo-control the laser in some way. From Fig. 2 it can be seen that adjustment either of the mirror separation L, or of the current I or of the pressure P will produce the desired stabilization of the output. The choice between these three servo loops will depend upon the environment and the technical expertise available. It is not sufficient simply to keep either L or I or P constant as the output will still suffer from fluctuations in the other two variables. Of course all three variables could be kept constant but this solution would be unnecessarily complicated and expensive.

9. Acknowledgments

The authors wish to thank the numerous research workers who have used HCN lasers at NPL[3] and have contributed to the body of knowledge regarding their behaviour. We gratefully acknowledge the assistance of the West Design Office of NPL in the mechanical design of various lasers. Lastly we wish to thank Mr. J. Hines, Mr. G. Neill, Mr. N. Cross and Mr. J. Hansen-Addy for their assistance in determining the stability characteristics of many different designs of laser.

10. References

1. Gebbie, H. A., Stone, N. W. B. and Finlay, F. D., 'A stimulated emission source at 0·34 millimetre wavelength', *Nature*, 202, p. 685, 16th May 1964.
2. Gebbie, H.. A, Stone, N. W. B., Chamberlain, J. E. and Shertaton, W. A., 'Submillimetre maser amplification and continuous wave emission', *Nature*, 211, p 62, 2nd July 1966.
3. Chantry, G. W. and Duxbury, G., 'Molecular lasing systems', in 'Methods of Experimental Physics', Vol. 2 (Ed. Professor Dudley Williams). (Academic Press, New York, to be published) Chantry, G. W., 'Submillimetre Spectroscopy—a Guide to the Theoretical and Experimental Physics of the Far Infra-Red' (Academic Press, London, 1971).
4. Fuller, D. W. E., Hines, J. and Compton, B., 'Short-term frequency stability of the HCN maser', *Electronics Letters*, 5, pp. 448–9, 18th September, 1969.

5. Bradley, C. C. and Knight, D. J. E., 'Absolute frequency measurement of a CF_2CH_2 absorption line near 890 GHz using an HCN laser', *Physics Letters*, **32A**, pp. 59–60, 1970.
6. Llewellyn Jones, D. J. and James, M. D., 'Stabilization of the HCN laser', *J. Phys.,E. (Sci. Instrum.)* **5**, pp. 468–72, May 1972.
7. Steffen, H. and Kneubuhl, F. K., 'Resonator interferometry of pulsed submillimeter-wave lasers', *I.E.E.E. Quantum Electronics*, **QE-4**, pp. 992–1008, December 1968.
8. Ono, S., Hotta, K. and Shibata, Y., 'Some experiments on the compact DC submillimetre laser', Proc. 8th Int. Conf. Microwaves and Optical Generation and Amplification, Sept 1970, pp. 21–24. Kluwer-Deventer (Netherlands).
9. Stafsudd, O. M. and Yeh, Y. C., 'The cw gain characteristics of several gas mixtures at 337 μ', *I.E.E.E. J. Quantum Electronics*, **QE-5**, pp. 377–80, July 1969.
10. Fuller, D. W. E. and Cross, N. R., 'Television display of HCN laser radiation', *Electronics Letters*, **8**, No. 2, p. **44**, 27th January 1972.
11. Holeman, B. R. and Wreathall, W. M., 'Thermal imaging camera tubes with pyroelectric targets'. *I.E.R.E.* Conference on Infra-Red Techniques, Reading, 21st–23rd September 1971. pp. 329–352. (I.E.R.E. Conference Proceedings No. 22).

Manuscript first received by the Institution on 14th June 1971 and in final form on 31st May 1972. (Paper No.1466/CC142.)

STANDARD FREQUENCY TRANSMISSIONS—July 1972

(Communication from the National Physical Laboratory)

July 1972	Deviation from nominal frequency in parts in 10^{10} (24-hour mean centred on 0300 UT)			Relative phase readings in microseconds N.P.L.—Station (Readings at 1500 UT)		July 1972	Deviation from nominal frequency in parts in 10^{10} (24-hour mean centred on 0300 UT)			Relative phase readings in microseconds N.P.L.—Station (Readings at 1500 UT)	
	GBR 16 kHz	MSF 60 kHz	Droitwich 200 kHz	GBR 16 kHz	†MSF 60 kHz		GBR 16 kHz	MSF 60 kHz	Droitwich 200 kHz	GBR 16 kHz	†MSF 60 kHz
1	—	0	+0·1	—	635·8	17	—	+0·1	+0·2	—	627·3
2	—	0	+0·1	—	636·5	18	—	+0·1	+0·1	—	626·0
3	—	0	+0·1	—	636·7	19	—	0	0	—	624·9
4	—	−0·1	+0·1	—	634·6	20	—	0	0	—	624·6
5	—	—	+0·1	—	—	21	—	+0·2	−0·1	—	622·6
6	—	—	+0·1	—	—	22	—	+0·1	0	—	622·0
7	—	—	+0·1	—	—	23	—	0	0	—	622·0
8	—	+0·1	+0·1	—	633·9	24	—	+0·1	−0·1	—	620·2
9	—	0	+0·1	—	633·6	25	—	+0·1	0	—	618 4
10	—	0	+0·1	—	632·4	26	—	—	—	—	—
11	—	+0·1	+0·1	—	631·7	27	—	—	—	—	—
12	—	0	+0·1	—	631·0	28	—	+0·1	0	—	617·2
13	—	+0·1	+0·1	—	630·5	29	—	+0·2	−0·1	—	615·6
14	—	+0·1	+0·2	—	629·3	30	—	+0·1	−0·1	—	614·8
15	—	+0·1	+0·1	—	628·5	31	—	0	−0·1	—	614·6
16	—	0	+0·2	—	628·3						

All measurements in terms of H.P. Caesium Standard No. 334, which agrees with the N.P.L. Caesium Standard to 1 part in 10^{11}.

† Relative to AT Scale; $(AT_{NPL} - \text{Station}) = +468{\cdot}6$ at 1500 UT 31st December 1968.

The GBR Transmitter at Rugby was off the air for maintenance during July.

U.D.C. 537.227: 621.383.4: 621.397.3

Pyroelectric Detector Arrays for Thermal Imaging

H. BLACKBURN, C.Eng., M.I.E.R.E.,*
H. C. WRIGHT, B.Sc.,*
R. EDDINGTON, L.R.I.C.*
and
R. S. KING, B.Sc.,*

Based on a paper presented at the Conference on Infra-red Techniques held in Reading from 21st to 23rd September 1971.

SUMMARY

The pyroelectric detector is well established as a very effective single-element infra-red detector operating at room temperature. This paper describes the development of linear arrays of detectors in which the detector elements and much of the circuitry required for their operation are in the same microelectronic package. To eliminate the effects of voltage offset variations in the pre-amplifiers a signal processing system has been developed which uses digital techniques.

* *Allen Clark Research Centre, The Plessey Company Limited, Caswell, Towcester, Northants.*

1. The Pyroelectric Detector

The pattern of self-luminescence from terrestrial objects is a consequence of the differences in black body radiation which arise from the small variations in absolute temperature and emissivity in the scene. Since the mean temperature will be about 300 K most of the radiation will be in the 10 μm wavelength region and an array of detectors can be used to observe the infra-red self-luminescence pattern and by suitable electronic processing to present a visible replica. Such thermal imaging systems are well served by bolometric detectors since a very fast response is not generally needed and the absence of detector refrigeration is a significant convenience. Thermal imaging work at these laboratories uses pyroelectric detectors made from crystals of triglycine sulphate (TGS), a material which shows a permanent electric dipole resulting in a surface charge.† This charge varies with temperature and hence, if regularly interrupted radiation falls on the TGS, a fluctuating charge appears across the crystal faces of the detector. As the crystal is highly insulating, the detector can be considered as a self-charging capacitor and it is easily incorporated into an electronic circuit.

Radiation from the source to be detected falls on the pyroelectric slice and is absorbed at or near the front face by an absorbing black electrode or else by the TGS itself after passing through an effectively transparent thin-film nichrome electrode. The radiation heats the pyroelectric layer and so charge appears at the electrodes. The charge output is proportional to the temperature change dT and so the current output into a low resistance is proportional to the rate of change in temperature, dT/dt. This means that the pyroelectric detector is useful where there are changes occurring in radiation flux and, if this does not naturally occur in the signal itself, then the incoming radiation must be chopped in some way.

2. Pyroelectric Arrays

Whenever an extended object is being imaged it is clearly an advantage to use more than one detector. Many applications, such as thermography require a two-dimensional form of display and therefore a two-dimensional form of array would be an advantage. In practice there are at the present time great difficulties in making all but very elementary two-dimensional thermal imaging arrays and so the emphasis has been on linear arrays of detectors. For many of the most potentially valuable applications this is no disadvantage at all as a moving object being viewed provides its own orthogonal scanning axis, as for example in monitoring the output of industrial mills or in aerial survey work, but when a two-dimensional image is required it is necessary to use an optical system scanning in one axis.

A linear detector array by itself would be very simple to make as it would consist simply of a long narrow strip of TGS with a common electrode on one face and a line of rectangular electrodes on the other face (Fig. 1) but because of the extremely high impedances involved

† Putley, E. H., 'Infra-red detectors', Chap. 6, in 'Semiconductors and Semimetals', Willardson, R. K. and Beer, A. C. (Eds.). (Academic Press, London, 1970).

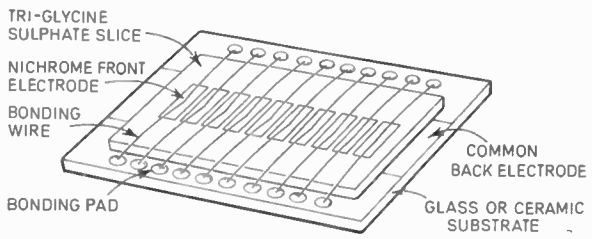

Fig. 1. TGS array.

it is necessary to have a preamplifier close to each detector and this means that the amplifier must be small. The m.o.s.t. integrated circuit process fills this requirement and it is easy to design a preamplifier that takes up no more width than a detector element, typically 0·025 cm.

The linear detector array is a thin continuous strip of TGS with a common electrode on one face and a line of rectangular electrodes on the other face. The front facing electrodes will in general be transparent to infrared so that the radiation is absorbed in the TGS itself.

The area of each electrode is governed by system requirements but clearly to give angular resolution with small aperture optics the detector area should be small, typically less than 10^{-3} cm^2. The thickness of the detector is determined by the required thermal time constant of the system which in turn depends on the chopping rate. A typical thickness is 0·005 cm, though thicknesses of 0·02 cm are useful for some applications.

The Plessey i.c. m.o.s.t. preamplifier uses a small-area m.o.s.t. as the active device and a large aspect ratio m.o.s.t. connected as a load resistor. To overcome the need for a biasing resistor a third m.o.s.t. is connected between the gate and drain of the active m.o.s.t. so that as leakage in the detector and m.o.s.t. tend to move the gate positive, away from the desired bias point, the third m.o.s.t. turns on very slightly and passes sufficient current to counterbalance the leakage. This circuit is very satisfactory when used at reasonably low signal levels. This preamplifier design used on the integrated circuit has an input capacitance of less than 1 pF, an input resistance higher than 10^{11} ohm and a voltage gain of 2·7. The output impedance of the single stage is rather high and so a source follower stage is included to bring the impedance down to less than 10 kΩ. It is convenient to have a block of eight preamplifiers side by side on one integrated circuit chip (Fig. 2). The circuit is available in this form but for array use it is desirable to have a single video output which carries all the information from the separate amplifiers. This involves a sampling system on the output of each preamplifier. The method used is to have an m.o.s.t. multiplexing switch on each output, the m.o.s.t. being switched sequentially by a parallel output shift register. One of the attractions of integrated circuits is that the eight multiplexers and the 8-bit shift register can be made readily and cheaply on the same chip as the eight preamplifiers. This sampling

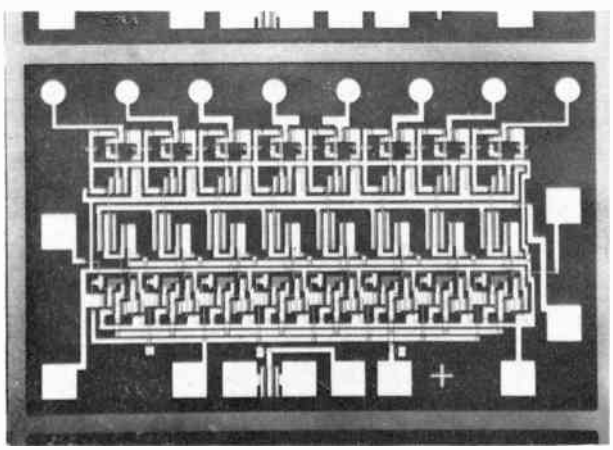

Fig. 2. M.o.s.t. integrated circuit.

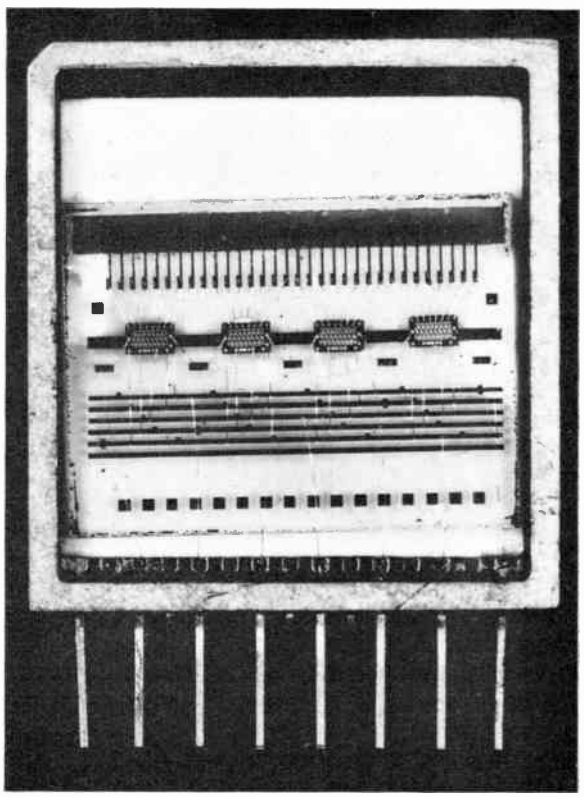

Fig. 3. 32-element array.

method becomes essential as the number of elements in the array increases. The output video signal requires a good deal of processing before it can be fed to the final stages of the display and this is described in the next section.

The integrated circuit and the detector array have to be connected together and this is achieved by mounting both the TGS and the integrated circuits onto a glass substrate on which has been deposited a gold-nichrome interconnexion pattern.

In one method of processing, the interconnexion pattern also serves to define the active area of the detector.

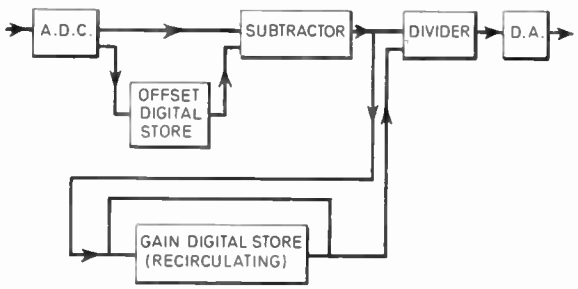

Fig. 4. Block diagram of spatial noise reduction system.

To do this a polished face of the TGS is bonded to the glass substrates by means of a very thin insulating layer of resin so that a capacitive coupling is made to the detector. Connexions to the integrated circuit are by conventional ultrasonic bonding but this will shortly be replaced by face-down flip-chip bonding.

A 32-element array with its four integrated circuits mounted inside a microelectronic package has been developed, the size of each detector being $0{\cdot}04 \times 0{\cdot}05$ cm (Fig. 3). The array is completed by sealing with a silicon window; this acts as a convenient filter to visible light which would otherwise generate a photocurrent in the m.o.s.t. integrated circuit. The responsivity and noise have so far been fully evaluated only in detectors with the relatively large area of $6{\cdot}4 \times 10^{-3}$ cm^2. Using the unmultiplexed circuit the responsivity at 125 Hz, referred to the preamplifier input, was typically 300 VW^{-1} and the noise was 3×10^{-6} V in one cycle bandwidth, giving a noise equivalent power of 10^{-8} W and a D^* of 8×10^6. This result was for the case of an unbloomed silicon window; allowing for the use of blooming and some improvements to conversion efficiency a D^* of 2×10^7 is a reasonable short-term target. The principal source of noise, at all but the lowest frequencies, is the voltage generator, or $1/f$, noise of the m.o.s.t. This is inversely proportional to the square root of the gate area of the m.o.s.t. and by optimizing this a further improvement should be possible.

3. Signal Processing

The outputs of any array system of detectors and amplifiers contain noise that is random with time and also random spatial variations due to differences in offset voltages in the amplifiers and gain variations of the amplifiers and detectors. Time-random noise cannot be eliminated by any following signal processing though its effect can be reduced by limiting the bandwidth if signal considerations allow this; spatial noise however is amenable to signal processing. The system developed for this work is conceptually based on techniques already developed for silicon opto-electronic arrays.

The required signal in a chopped radiation system is the difference in level of the signal at the end of the 'light' phase of the chopping cycle and that at the end of the next 'dark' phase. In order to do this subtraction it is necessary to delay the signal for half a chopping cycle so that the two phases can be compared. In this way the effect of any offset errors in the amplifiers is eliminated, (Fig. 4). The method used is to convert the analogue

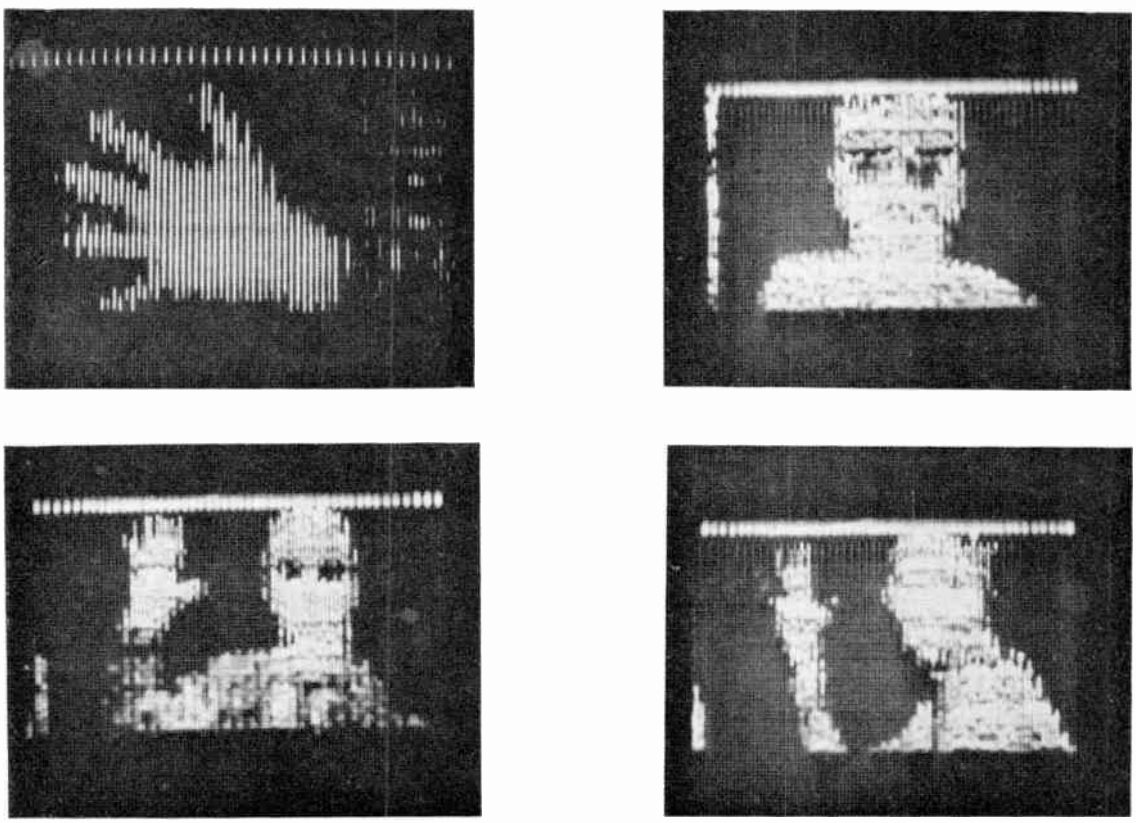

Fig. 5. Thermographs using 32-element arrays.

video signal to digital form and store the ten resulting bits of information in ten parallel shift registers whose length is equal to the numbers of detectors in the array. Thus if the detector outputs are sampled twice in every chopping cycle at the points of peak signal level then the delayed signal becomes available at the end of the parallel store just as the equivalent signal of the opposite phase is converted to digital information. By the use of a digital subtractor and a following digital-to-analogue converter the output of the processor is freed of offset errors. The system is capable of processing signal levels of 1 mV in the presence of offset variations of 1 V; a 1000 to 1 improvement. The technique is proving of very great value for several types of array which previously would have been impractical. The system is currently being extended to correct for responsivity variations. Once the signal has been converted to digital form a great deal of sophisticated signal processing becomes available. It is important to emphasize that such techniques use commercially-available integrated circuits and that the cost of such processing systems is therefore not great compared with the rest of an imaging system.

4. Conclusions

The main emphasis of the work in pyroelectrics has been in the development of single elements and linear arrays with their associated circuitry and signal processing. Complete thermal imaging systems have also been built which show considerable promise. Using a fairly conventional optical system with optical scanning in one axis, thermograms have been obtained with 32-element arrays (Fig. 5) and the system is being extended to arrays of 128 elements. As the noise levels are reduced still further by the use of more fully developed signal processing systems and lower noise preamplifiers this uncooled form of detector array will provide high resolution thermography in a convenient and rugged form.

5. Acknowledgments

This work was supported by the Ministry of Defence (Procurement Executive). The authors are grateful to the Directors of The Plessey Company Limited for permission to publish the paper.

Manuscript first received by the Institution on 29th June 1971 and in final form on 21st April 1972. (No. 1467/CC143.)

U.D.C. 621.372.573.2.029.45

The Design of an Audio-frequency Active RC Band-pass Filter for a Specific Engineering Requirement

D. G. HAIGH, B.Sc.*

and

R. JEFFERS, B.Sc.†

SUMMARY

An engineering requirement for an audio-frequency band-pass filter can be met with an active RC filter which uses positive impedance convertors to simulate the inductors of an LC filter. Because of the low sensitivity of this type of realization, the component tolerances required are compatible with thick film technology.

* *Formerly with the Hirst Research Centre, now in the Electrical Engineering Department, Imperial College of Science and Technology, London SW7 2BT.*

† *The General Electric Co. Ltd., Telecommunications Research Laboratories, Hirst Research Centre, Wembley, Middlesex, HA9 7PP.*

1. Introduction

A requirement arose for an audio-frequency band-pass filter operating between 600 Ω resistive terminations, and meeting the amplitude/frequency specification shown in Fig. 1. Either the filter must be capable of transmission in both directions or two filters must be provided, one for transmission and one for reception.

An active RC realization was required because of a volume restriction on the filter, and it was envisaged that ultimately a microelectronic realization might be used.

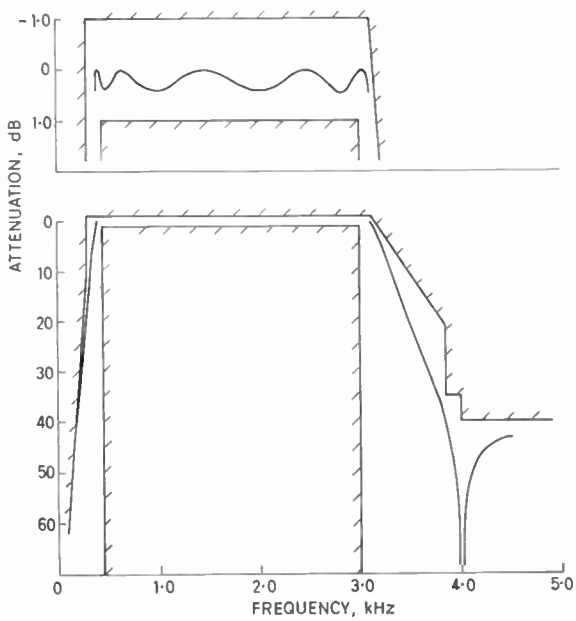

The filter response is required to lie within the bounds shown on the diagram. The important points are as follows:

Frequency	Required attenuation
0·25 kHz	greater than 20 dB
0·3 kHz	greater than 12 dB
0·44 to 3·0 kHz	between ±1 dB
3·84 kHz	greater than 35 dB
4·0 to 200 kHz	greater than 40 dB

Fig. 1. Specification of amplitude/frequency response and chosen approximating function.

2. Active RC Realization

Regardless of which realization technique is employed, it is first of all necessary to find a real rational function of the complex frequency variable 'p' which will meet the specification. It was decided to use a transfer function which had an amplitude/frequency response with an equi-ripple pass-band. The method of obtaining such a function is given by Bingham.[1] The amplitude/frequency response of the selected function is shown in Fig. 1, where it can be seen that only about 0·5 dB of the 2 dB permissible pass-band variation has been used up, the remainder being available for changes due to component tolerances, ageing, etc. The selected function was of tenth order and had a pair of finite transmission zeros and four zeros at infinite frequency.

Many methods of active realization of a given transfer function are available.[2] The following two methods which have been found by the authors to be particularly useful and which are reviewed in more detail by Saraga,[3] will be briefly considered.

2.1. *Cascade Connexion of Biquadratic Sections*

In this method, the transfer function is split into biquadratic factors, each of which is realized by a separate active RC section. The filter then consists of a cascade of these sections each of which can usually be realized using one operational amplifier. However transmission is possible in only one direction and it follows that for the present application two filters would be required each containing five sections giving a total of ten amplifiers. The main disadvantage of the cascade type of realization is that the amplitude response of the filter is very sensitive to changes in the resonant frequencies of individual sections. It can be shown that for sections which would be suitable in the present application, a 1% change in resonant frequency would cause a 0·9 dB change in the amplitude response of the filter. This 1% change in resonant frequency would typically be caused by a 2% change in any one of several components.

2.2. *Active Simulation of Inductors in an LC Filter*

In this method an LC filter of the ladder type is designed to have the required transfer function. The inductors are then simulated in some way using active RC networks. The advantage of this technique is that low sensitivity to component tolerances, such as that inherent in LC ladder networks,[4] can be approached. Two inductance simulation methods are suitable for the realization of the required transfer function, one using gyrators[4] and the other positive impedance convertors[5] (p.i.c.s). Since it is possible to transmit through these filters in either direction, the present requirement could be met using one such filter.

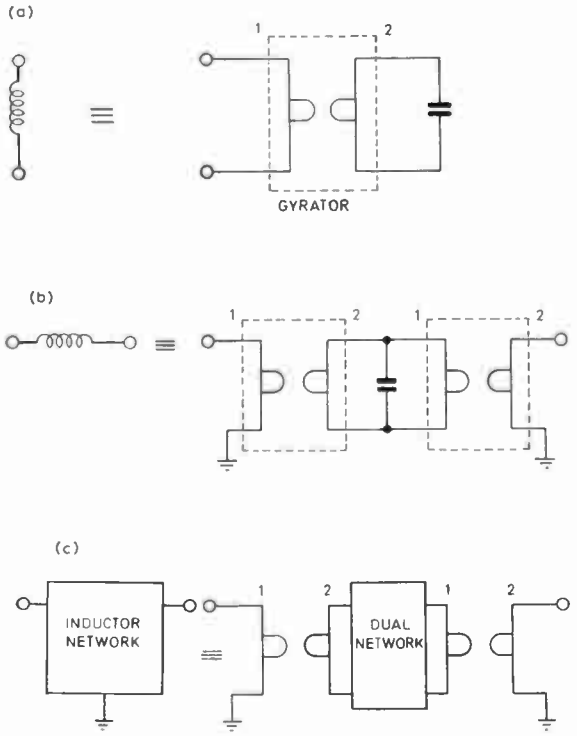

Fig. 2. Simulation of inductors using gyrators.

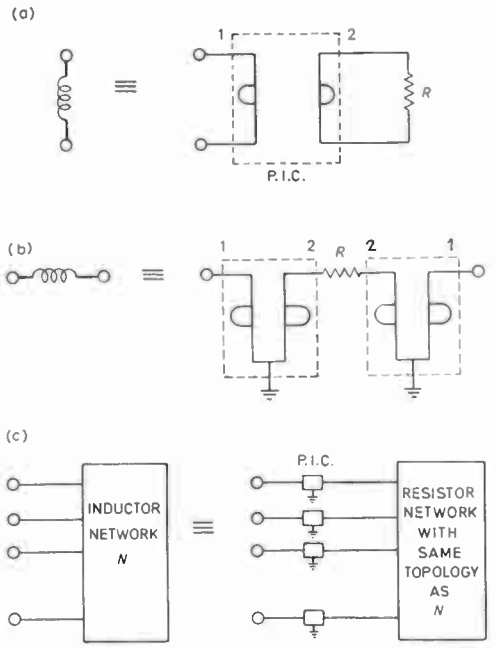

Fig. 3. Simulation of inductors using p.i.c.s.

A gyrator is a two-port network which has the property that the impedance seen at one port is proportional to the inverse of the impedance connected to the other port. Thus an inductor may be replaced by a gyrator terminated in a capacitor as shown in Fig. 2(a). Practical gyrators usually have one of their input terminals connected to the d.c. power supply, so if we wish to have several gyrators fed from the same d.c. supply, it is necessary that the inductors being simulated have a common terminal. Hence, no problem arises with grounded inductors (which share the signal earth as a common terminal), but to realize a floating inductor a circuit using two identical grounded gyrators[6] as shown in Fig. 2(b) is required. In general, an inductor two-port network may be replaced by its dual network seen through two identical gyrators, as shown in Fig. 2(c). This may allow a smaller number of gyrators to be used than that which would be required using Figs. 2(a) and (b).

A p.i.c. is a two-port network which has the property that the impedance seen at one port is directly proportional to the impedance connected to the other port. If the proportionality factor is chosen to be a constant multiplied by the complex frequency variable, then an inductive impedance is seen at one port when the other port is terminated in a resistor as shown in Fig. 3(a). In practice the p.i.c. has similar earthing problems to the gyrator and a three terminal p.i.c. is normally used. The realization of a floating inductor requires the use of two identical p.i.c.s as shown in Fig. 3(b). The significant difference between the p.i.c. and the gyrator becomes apparent in the simulation of an n-terminal inductor network. This is achieved, using p.i.c.s, by replacing the inductor network by a resistor network of identical

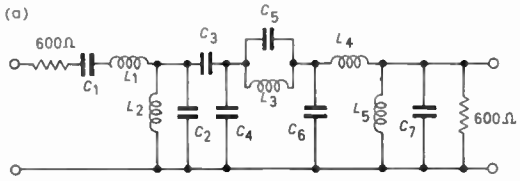

$C_1 = 0{\cdot}3560\ \mu F$ $C_7 = 0{\cdot}1642\ \mu F$
$C_2 = 69{\cdot}447\ nF$ $L_1 = 59{\cdot}10\ mH$
$C_3 = 0{\cdot}3012\ \mu F$ $L_2 = 0{\cdot}1701\ H$
$C_4 = 36{\cdot}230\ nF$ $L_3 = 37{\cdot}87\ mH$
$C_5 = 41{\cdot}802\ nF$ $L_4 = 45{\cdot}01\ mH$
$C_6 = 0{\cdot}1351\ \mu F$ $L_5 = 0{\cdot}1281\ H$

(a) LC filter.

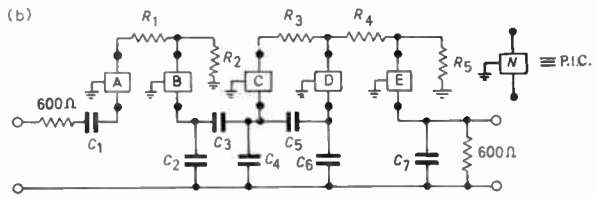

$R_1 = 11{\cdot}82\ k\Omega$ $R_4 = 9{\cdot}002\ k\Omega$
$R_2 = 34{\cdot}02\ k\Omega$ $R_5 = 25{\cdot}62\ k\Omega$
$R_3 = 7{\cdot}574\ k\Omega$

(b) Filter with simulated inductors.

Fig. 4.

topology and looking in at the ports through identical p.i.c.s as shown in Fig. 3(c). Note that the resistor values have a one-to-one correspondence to the inductances they are simulating.

Gyrators and positive impedance convertors can be realized by circuits having two operational amplifiers.[7] Using either technique in the present application, the total number of amplifiers required would be expected to be ten, since five inductors would be required.

2.3. *Assessment of Alternative Methods*

After considering the various methods discussed above it was decided to use the p.i.c. method. The cascade connexion of biquadratic sections method was discounted because the number of amplifiers required would be similar to that needed for an inductance simulation method and the sensitivity would be expected to be worse. The p.i.c. method of inductance simulation was chosen in preference to the gyrator method, because, a reliable three terminal p.i.c. circuit was known, and the design of the resistor network and the tuning of the resulting filter are made easy by the one-to-one correspondence which exists between resistors and simulated inductors.

An LC filter suitable for p.i.c. simulation of the inductors was designed from the required transfer function. The particular structure was chosen because the number of p.i.c.s required is a minimum (namely five). The LC circuit is shown in Fig. 4(a), and Fig. 4(b) shows this circuit with the inductor sub-networks replaced by p.i.c.s and corresponding resistor sub-networks.

3. Positive Impedance Convertor Circuit

A positive impedance convertor, as used here, is a two-port network with transmission matrix given by:

$$[T] = \begin{bmatrix} 1 & 0 \\ 0 & \dfrac{1}{pk} \end{bmatrix}$$

where the transmission matrix is defined by:

$$\begin{bmatrix} V_1 \\ I_1 \end{bmatrix} = [T] \begin{bmatrix} V_2 \\ I_2 \end{bmatrix}$$

the conventions for voltage and current being shown in Fig. 5(a). If a resistor R is connected to port 2 then the impedance presented at port 1 is that of an inductor L where $L = kR$. The factor k is termed the conversion ratio of the p.i.c. When p.i.c.s are used to simulate an inductor network by converting a resistor network, then the p.i.c.s used must have identical conversion ratios and each inductor value is then given by k times the corresponding resistor value.

A suitable realization of a p.i.c. is shown in Fig. 5(b). This circuit has been used by Antoniou.[7] The conversion ratio k is given by:

$$k = \frac{C_N R_{1N} R_{3N}}{R_{2N}} \qquad \text{.....(1)}$$

This circuit was constructed using integrated operational amplifiers, type μA741, with the component values as shown.

Using ideal operational amplifiers this would give $k = 5 \times 10^{-6}$. However, in practice an error in k was found, which was due to imperfections in the operational amplifiers. It was found that in order to return k to its correct value, R_{3N} should be adjusted to about 9·6 kΩ.

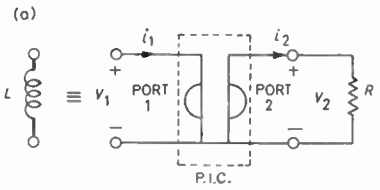

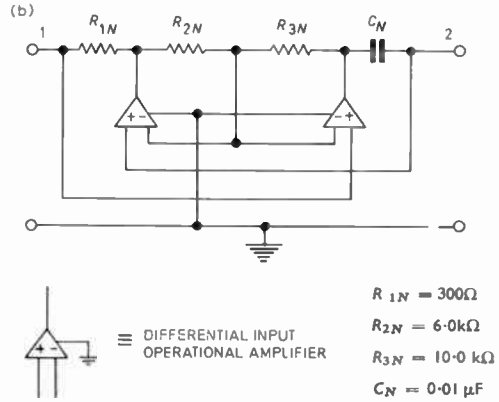

Fig. 5. Positive impedance convertor circuit.

The value of the conversion ratio was chosen to give reasonable values for the resistor sub-network. The choice of R_{1N}, R_{2N}, R_{3N} and C_N affects the signal handling capability of the filter and the values were chosen empirically to give a compromise between good signal handling and reasonable component values.

4. Construction, Measurement and Tolerancing of the Filter

A discrete component laboratory model was constructed using μA741 operational amplifiers, Metox resistors, and a combination of polystyrene and polyester capacitors. All components were made accurate to 0·1 %. The resistors R_{3N} of the p.i.c.s were made variable and each p.i.c. was set up to have the correct conversion ratio. The setting-up procedure was as follows. Each

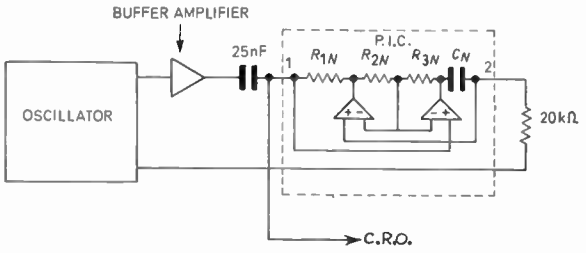

Fig. 6. Set-up used for adjusting p.i.c.s.

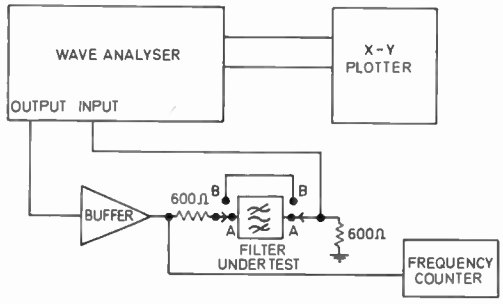

Fig. 7. Measuring set-up.

p.i.c. was terminated at port 2 in a standard resistor (20 kΩ) and the inductance presented at port 1 was connected in series with a standard capacitor (25 nF) as shown in Fig. 6. R_{3N} was adjusted until resonance occurred at the correct frequency which was calculated from the standard resistor and capacitor values and the required value of k. For $k = 5\times10^{-6}$ the required resonant frequency is 3183 Hz. The Q-factors of the simulated inductors were of the order of 300.

All measurements were made using a Hewlett–Packard wave analyser type 3590A with sweeping local oscillator plug-in type 3595A, in conjunction with an X-Y plotter (Fig. 7). The switch position B is used for setting up a 0 dB amplitude reference on the X-Y recorder. The decibel scale on the recorder is set up with the filter replaced by a 600 Ω variable attenuator. The frequency scale is set up using the frequency counter. During measurements the bandwidth of the wave analyser was normally set to 100 Hz and the sweep speed to 100 Hz/s.

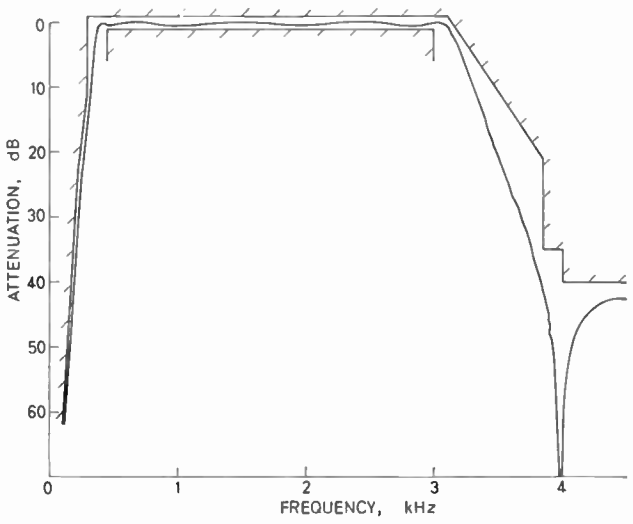

Fig. 8. Measured response.

The amplitude/frequency response of the filter was measured and is shown in Fig. 8, together with the specification. Figure 9 shows that changes in supply voltage and temperature have very little effect on the filter pass-band.

It was decided that, to assist in the tolerancing of the filter, the change in the response curve due to a change in a component value should be measured for each component individually. Distinction should be made between components which correspond to components in the original LC filter and those which do not. Capacitors C_1–C_7 are the original capacitors of the LC filter and resistors R_1–R_5 correspond to the original inductors. Changes in the pass-band response curve due to individual changes in these components are shown in Fig. 10. The remaining passive components are all part

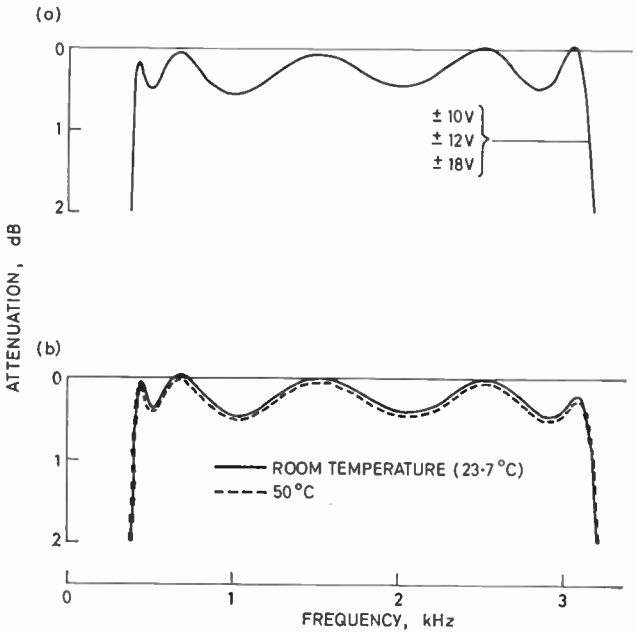

Fig. 9. (a) Effect of variation of supply voltage.
(b) Temperature sensitivity.

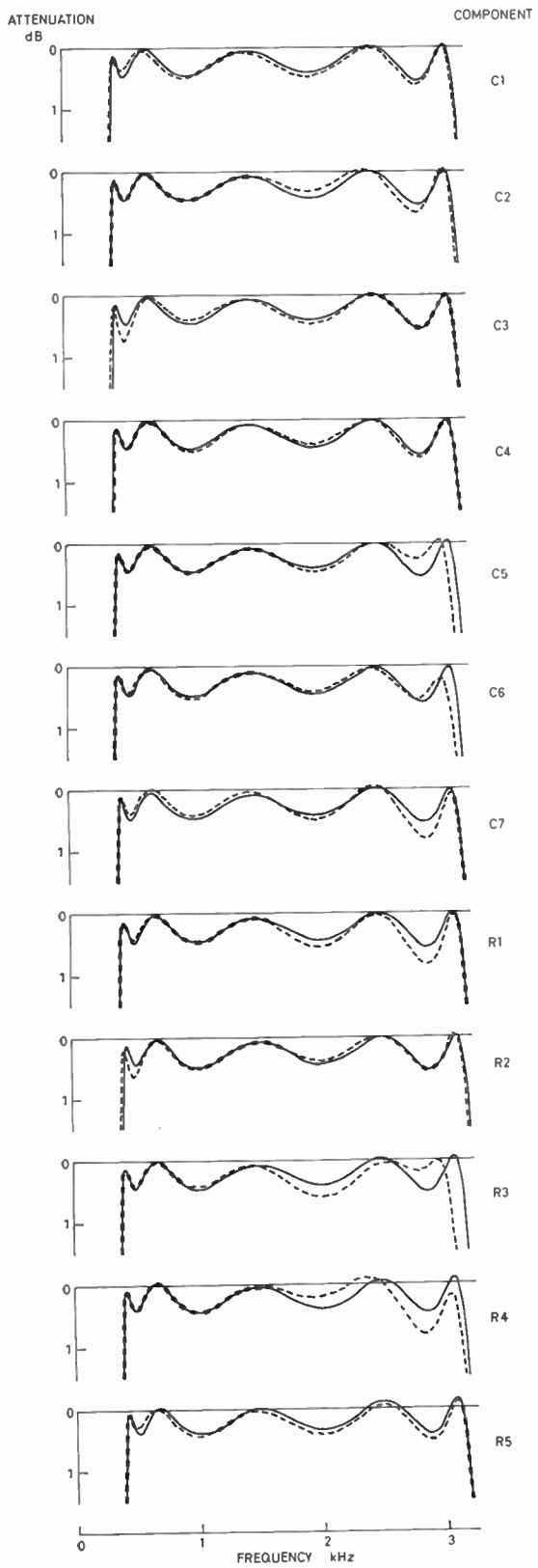

Fig. 10. Effect of 10% increases in components.
——— nominal
------- +10%

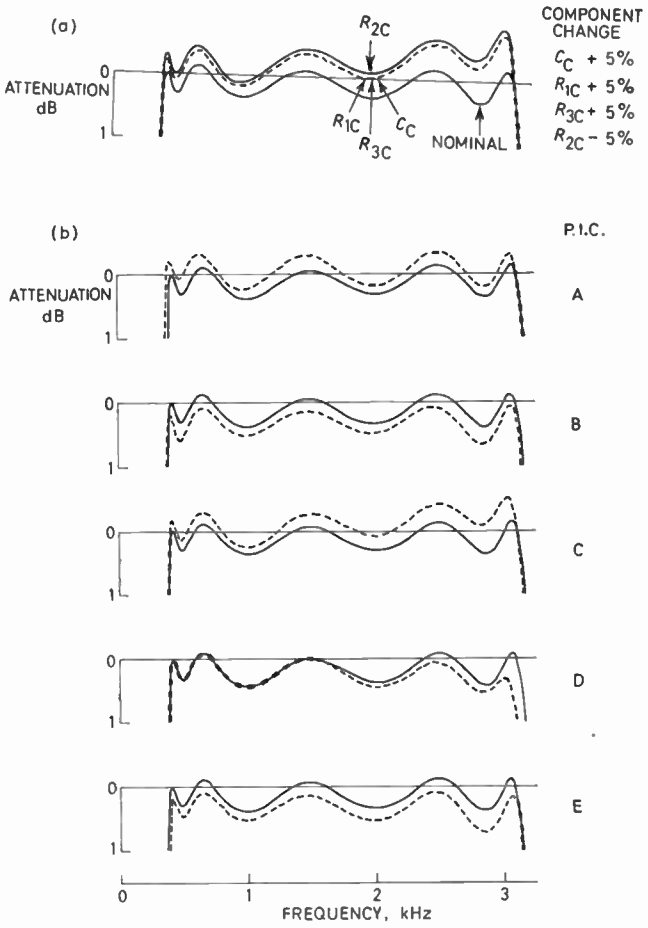

Fig. 11. (a) Effect of 5% changes in the components in p.i.c. (C). (b) Effect of 5% increases in each p.i.c. conversion ratio.

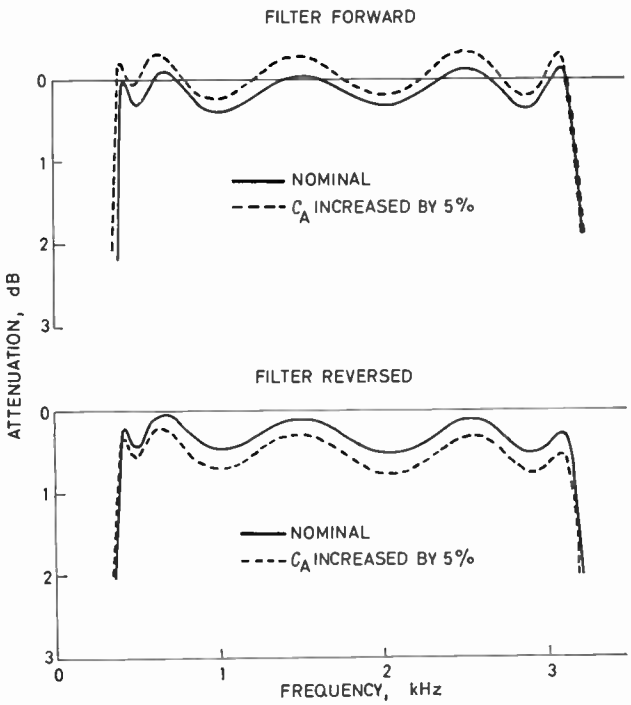

Fig. 12. Effect of changing C_A with filter reversed.

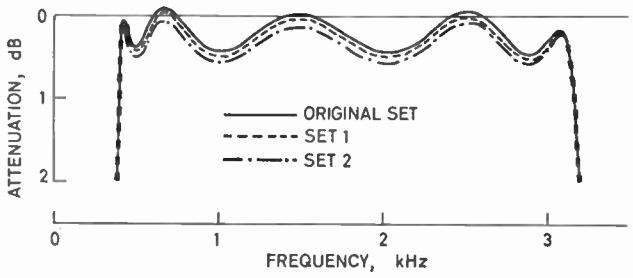

Fig. 13. Effect of replacing original amplifiers by sets chosen at random.

of the p.i.c. units and changes in these components will only change the conversion ratio of the corresponding p.i.c. as shown by equation (1). Therefore, the effects of changing R_{1N}, R_{3N} and C_N should be identical and opposite to the effect of changing R_{2N}. This was confirmed by measurements for p.i.c. (C), as shown in Fig. 11(a). Complete tolerance information for the components in the p.i.c. was therefore obtained by changing only the capacitor in each p.i.c. Graphs of changes in response curve for changes in each of these capacitors are shown in Fig. 11(b). Figures 10 and 11 illustrate the low sensitivity to component variations claimed for this type of realization in Section 2.2.

At this point it is important to consider how the filter behaves when it is used in the reverse direction. It is well known that an LC filter has the same response when used in either direction. Provided the conversion ratios of the p.i.c.s are closely matched, the present active filter will behave in the same manner as an LC filter. However, when we change the conversion ratios of individual p.i.c.s the active network is no longer equivalent to an LC filter and, in general, we would expect the effect of these changes to depend on the direction in which the filter is used. This is illustrated by Fig. 12 which shows the response of the filter measured in both directions for a 5% change in the conversion ratio of p.i.c.(A).

A difficulty arises when we attempt to set tolerances on the amplifiers used in the filter. This is because each amplifier is described by several parameters, changes in any of which may have an effect on the response. Therefore, an empirical approach was adopted. A nominal response curve was plotted and compared with the response obtained when a new set of amplifiers was used. This was repeated using a second new set of amplifiers. The results shown in Fig. 13 indicate the relative insensitivity of this filter to amplifier changes.

The ultimate object of making the above measurements was to derive a tolerance figure for each component which will ensure that the filter always remains within the specification. The sensitivity curves (Figs. 10 and 11) were used to select tentative tolerance figures for the components. These tolerances were tested by choosing combinations of component changes within them which would be most likely to put the response outside specification. In order to select these combinations, certain assumptions were made about the effect of simultaneous changes in components. These assumptions are best explained with reference to Fig. 14. If changing a component by $y\%$ causes an amplitude deviation as shown in Fig. 14(a) then changing it by $-y\%$ is assumed to make the opposite deviation as shown in that Figure. Again if a component changed by $y\%$ causes a tuning deviation as shown in Fig. 14(b), then changing it by $-y\%$ is assumed to make an opposite tuning deviation as shown in the Figure. An experimental verification of these assumptions for C_5 is given in Fig. 14(d). The type of change shown in Fig. 14(c) applies to changes of $y\%$ in p.i.c. conversion ratios. An experimental verification of this is given in Fig. 14(e). It is assumed that the total change in the response curve caused by several components being changed simultaneously will be predictable by considering the combined effect of individual changes.

Using this technique a set of tolerances was obtained, which are shown on the circuit diagram of the complete filter (Fig. 15). The worst case response curves using these tolerances are shown in Fig. 16. In Fig. 16(a) the signs of the tolerances have been chosen so as to give maximum error in the loss. In Fig. 16(b) the signs are such that the upper cut-off frequency is increased and decreased by the maximum amount. Although these curves do not quite meet the specification it was decided that they were acceptable, since the worst cases were unlikely to occur.

5. Microelectronic Realization

The tolerances given in Fig. 15 are compatible with present-day thick film realization using close tolerance chip capacitors, and flat-pack operational amplifiers.

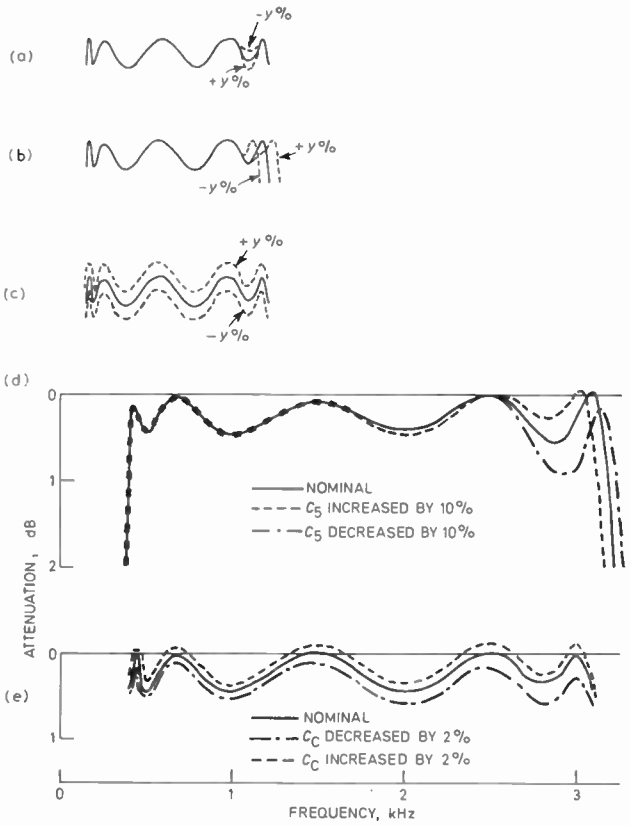

Fig. 14. Assumptions used for tolerancing.

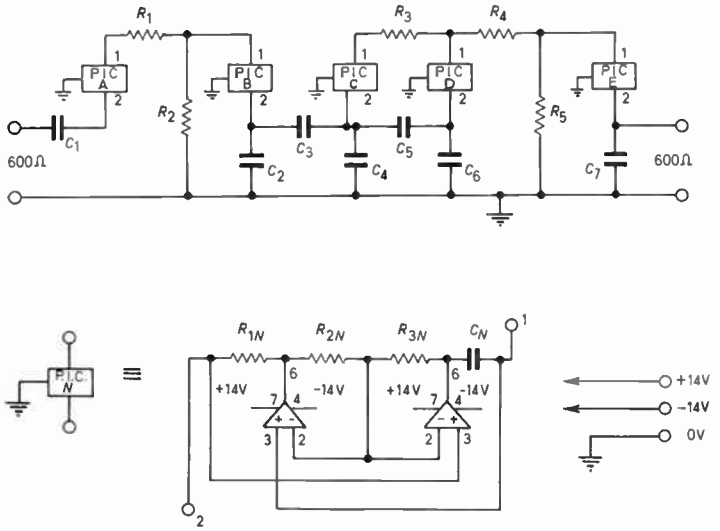

Fig. 15. Circuit diagram of filter.

Component	Value	Tolerance ± %
R_1	11·82 kΩ	3
R_2	34·02 kΩ	3
R_3	7·574 kΩ	2
R_4	9·002 kΩ	2
R_5	25·62 kΩ	3
C_1	0·356 μF	5
C_2	0·069447 μF	5
C_3	0·3012 μF	5
C_4	0·03623 μF	5
C_5	0·041802 μF	2
C_6	0·1351 μF	2
C_7	0·1642 μF	5
R_{1N}	0·3 kΩ	Tolerance on $\frac{R_{1N}.R_{3N}.C_N}{R_{2N}}$ is ±2%
R_{2N}	6 kΩ	
R_{3N}	9 kΩ → 10 kΩ*	
C_N	0·01 μF	

N = A, B, C, D, E

* Exact value depends on amplifier used.

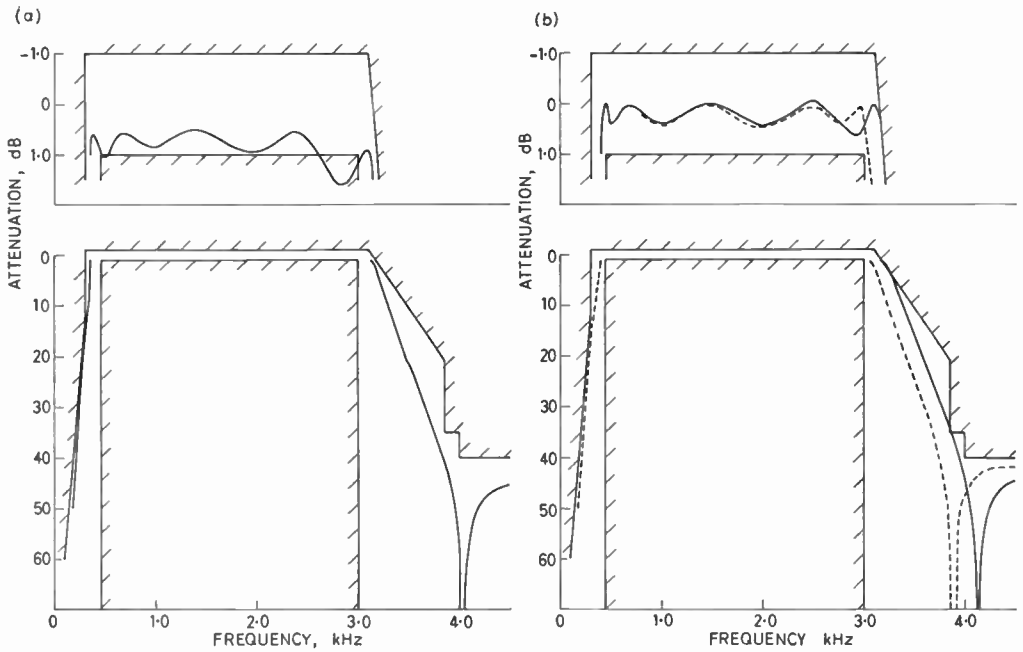

(a) Worst case response for maximum error in pass-band loss.

C_3+5%	R_4+2%
C_5−2%	C_A−2%
C_7+5%	C_B+2%
R_1+3%	C_C−2%
R_2+3%	C_D+2%
R_3−2%	C_E+2%

(b) Worst case response for maximum errors in upper cut-off frequency.

C_5+2%	C_5−2%
C_6+2%	C_6−2%
R_3+2%	R_3−2%
R_4+2%	R_4−2%
C_D+2%	C_D−2%

Fig. 16.

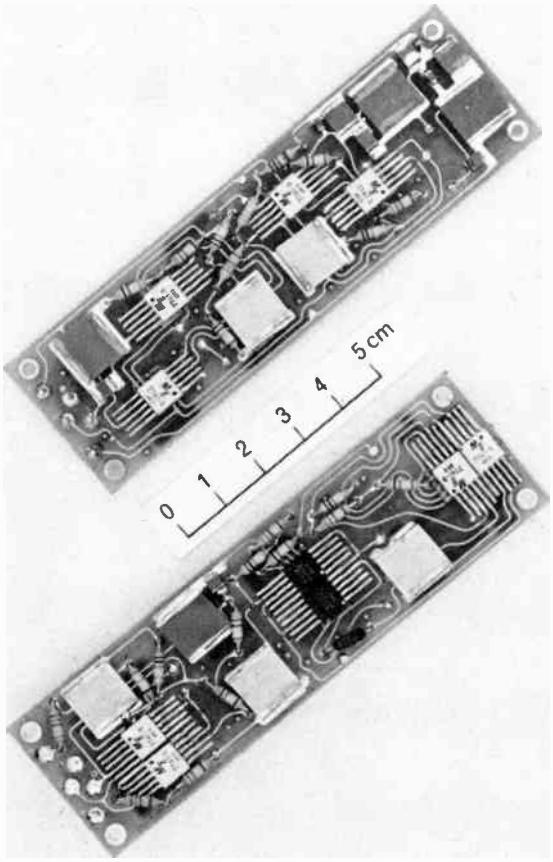

Fig. 17. Printed circuit board model of the filter.

Preliminary discussions with a view to obtaining some thick film models indicate that the final volume of the filter would be about $6{\cdot}4 \times 5{\cdot}1 \times 0{\cdot}5$ cm ($2{\cdot}5 \times 2 \times 0{\cdot}2$ in). For laboratory purposes a miniature printed circuit board version of the filter was constructed (size $10{\cdot}8 \times 3{\cdot}2 \times 0{\cdot}76$ cm or $4{\cdot}25 \times 1{\cdot}25 \times 0{\cdot}3$ in) and a photograph of this is shown in Fig. 17. This uses ceramic chip capacitors, flat-pack operational amplifiers and miniature resistors. Both sides of the printed circuit board are shown in the photograph.

6. Conclusions

A specific requirement for an audio-frequency bandpass filter has been studied, and it has been shown that the engineering specifications can be satisfied using an active RC realization.

It is thought that the results presented here show that quite sophisticated filter designs are amenable to active RC realization. The utilization of such active RC filters is dependent on the cost of microelectronic circuitry.

7. Acknowledgments

The authors would like to acknowledge helpful discussions with Dr. W. Saraga and the assistance of Mr. M. A. Kunes who made all the measurements.

8. References

1. Bingham, J. A. C., 'The approximation problem for both conventional and parametric bandpass filters', *Trans. Inst. Elect. Electronics Engrs on Circuit Theory*, **CT-11**, p. 408, September 1964.
2. Mitra, S. K., 'Analysis and Synthesis of Linear Active Networks' (John Wiley, New York, 1969).
3. Saraga, W., 'Frequency-selective networks suitable for microelectronic realization', *J. Science and Technology*, **38**, No. 3, pp. 128–38, 1971.
4. Orchard, H. J., 'Inductorless filters', *Electronics Letters*, **2**, No. 6, pp. 224–5, June 1966.
5. Gorski-Popiel, J., 'RC-active synthesis using positive immittance convertors', *Electronics Letters*, **3**, No. 8, pp. 381–2, August 1967.
6. Holt, A. G. J. and Taylor, J., 'Method of replacing ungrounded inductors by grounded gyrators', *Electronics Letters*, **1**, No. 1, p. 105, June 1965.
7. Antoniou, A., 'Realization of gyrators using operational amplifiers and their use in RC-active-network synthesis', *Proc. Instn Elect. Engrs*, **116**, pp. 1838–50, December 1969.

Manuscript first received by the Institution on 14th March 1972 and in final form on 1st June 1972. (Paper No. 1468 /CC144.)

U.D.C. 621.382.23.3.011.4

Measurement of Varactor Capacitance Parameters

R. B. SMITH, Ph.D., C.Eng., M.I.E.E.*
and
B. BRAMER, Ph.D.*

SUMMARY

A new technique is proposed for the determination of the parameters of the capacitance-voltage relationships of the p-n junction varactor. Special charts are used in conjunction with the measured values of varactor capacitance at five bias voltages. The determination of the Fourier capacitance coefficients of the pumped varactor is then discussed, another chart being used, in conjunction with the parameters of the capacitance-voltage relationship, to determine values for these coefficients. The chart is applicable to voltage and current pumping. Experimentally-determined capacitance coefficients are compared with those obtained using the chart.

* *University of Bradford, Postgraduate School of Electrical and Electronic Engineering, Bradford 7.*

List of Principal Symbols

C_d	small-signal depletion-layer capacitance
$C_{d(0)}$	depletion-layer capacitance at zero bias voltage
C_k	kth capacitance coefficient of the pumped varactor
C_m	measured capacitance
C_0	average capacitance coefficient of the pumped varactor
C_s	stray capacitance of varactor encapsulation
$C(t)$	time-dependent capacitance
n	exponent of capacitance-voltage relationship
Q_d	ionic space charge on p-side of junction
$Q_{d(0)}$	ionic space charge at zero bias voltage
Q_i	injected charge
v	instantaneous pump voltage
V_b	d.c. bias voltage
V_p	pump voltage amplitude
α	generalized exponent
β	pump amplitude coefficient
γ_k	kth gamma coefficient of the pumped varactor
ϕ	diffusion potential
ω_p	pump angular frequency

1. Introduction

Assumed values of the capacitance coefficients of the pumped varactor are generally used to predict the performance of parametric amplifiers.[1,2] To determine values for these coefficients, the relationship between the small-signal depletion-layer capacitance and the bias voltage, as well as the pump waveform must be known.

In this paper a new technique for finding the parameters of the capacitance-voltage relationship is described, and these paremeters are then used to determine the capacitance coefficients of the pumped varactor. The technique makes use of specially constructed charts which enable the diffusion potential, ϕ, and the junction exponent, n, to be found directly from the measured capacitance at five specific bias voltages. The technique eliminates the lengthy computer calculations of the method proposed by Bajon, Hoffman and Hait,[3] and the measurement of the slope of the varactor capacitance-voltage relationship required in methods previously proposed by the authors.[4,5] In Section 5, the parameters are used to find values for the capacitance coefficients of the pumped varactor for both current and voltage pumping. In these calculations it is not possible to assume that the exponent, n, has an integer value. Graphical and experimental verification of the calculated coefficients are the subjects of Sections 6 and 7 respectively. Experimental results are given for silicon and gallium arsenide varactors.

2. Capacitance-Voltage and Capacitance-Charge Relationships

If under conditions of reverse bias voltage, V_b, the depletion-layer is assumed to be free of mobile charge carriers and to be well defined, the negative ionic space charge, Q_d, on the p-side of the junction is given by[6]

$$Q_d = -Q_{d(0)}(1 - V_b/\phi)^{(n-1)/n} \qquad \ldots\ldots(1)$$

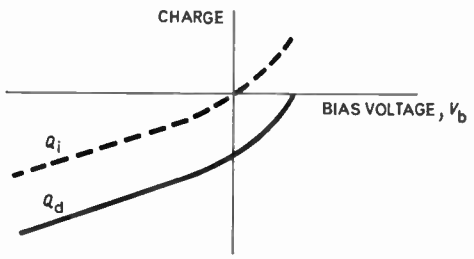

Fig. 1. Charge-voltage relationships. Q_d is the total charge on the p-side of the junction, and Q_i is the corresponding injected charge.

Here, $Q_{d(0)}$ is the magnitude of the fixed ionic space charge at $V_b = 0$, ϕ is the diffusion potential, and n an exponent whose value depends upon the doping profile in the vicinity of the junction. The parameters are assumed to be voltage independent. The form of the charge-voltage relationship is shown in Fig. 1. The small-signal depletion-layer capacitance, C_d, is found by differentiation of equation (1) and hence

$$C_d = C_{d(0)}(1 - V_b/\phi)^{-1/n} \qquad \text{.....(2)}$$

where

$$C_{d(0)} = \frac{n-1}{n}\frac{Q_{d(0)}}{\phi} \qquad \text{.....(3)}$$

is the depletion-layer capacitance at $V_b = 0$.

Analysis[7] based on the 'non-deplete' nature of the depletion layer leads to an expression relating, the depletion-capacitance to voltage, which is physically more precise. However, the measurements discussed in this paper show that equation (2) can be used for an accurate description of the capacitance-voltage relationship, although the values obtained for the parameters are not necessarily the true physical values.

It is seen from Fig. 1 that the charge, Q_i, injected into the p-side of the junction is given by

$$Q_i = Q_{d(0)} + Q_d \qquad \text{.....(4)}$$

On substitution for Q_d from equation (1) this can be written

$$(1 - Q_i/Q_{d(0)})^{-1/(n-1)} = (1 - V_b/\phi)^{-1/n} \qquad \text{.....(5)}$$

The depletion-layer capacitance can then be expressed as a function of injected charge. Thus,

$$C_d = C_{d(0)}(1 - Q_i/Q_{d(0)})^{-1/(n-1)} \qquad \text{.....(6)}$$

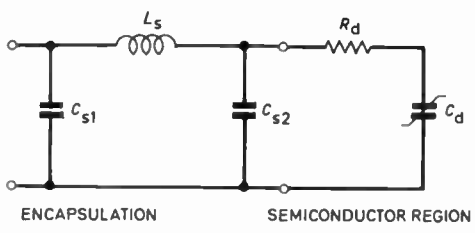

Fig. 2. Equivalent circuit of the encapsulated varactor.
C_d depletion-layer capacitance
R_d series-loss resistance
L_s stray inductance
C_{s1}, C_{s2} stray capacitances

An equivalent circuit of the encapsulated varactor is shown in Fig. 2. A lumped circuit representation of the semiconductor region of a varactor is valid since its dimensions are small compared with wavelength for all frequencies at which it is used, and generally skin effect and surface effects can be neglected. The dimensions of the encapsulation are, however, comparable with wavelength and a distributed equivalent circuit should therefore be used, although the π-equivalent circuit of Fig. 2 is used. At a frequency of 1 MHz, R_d and the reactance of L_s are both small compared with the reactances of C_d, C_{s1} and C_{s2} (see Fig. 2). The measured capacitance at this frequency is therefore given by

$$C_m = C_s + C_{d(0)}(1 - V_b/\phi)^{-1/n} \qquad \text{.....(7)}$$

where $C_s = C_{s1} + C_{s2}$ is the total stray capacitance of the encapsulation.

3. Experimental Determination of the Parameters $C_{d(0)}$, C_s, ϕ and n

A chart is constructed from which values for ϕ and n can be read directly if the value of C_m is known at five specific bias voltages. Consideration of equation (7)

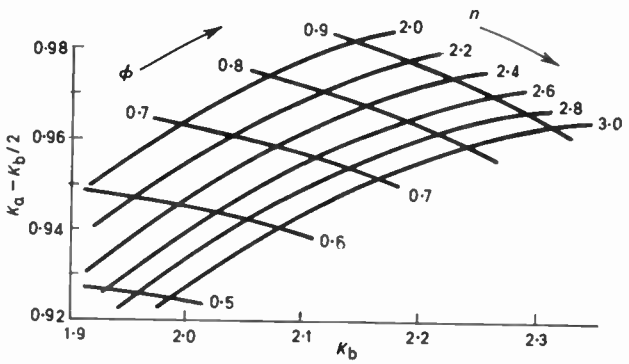

Fig. 3. Chart for the capacitance-voltage parameters of silicon varactors. $V_1 = -0{\cdot}1$ V, $V_2 = -1{\cdot}25$ V, $V_3 = -0{\cdot}5$ V, $V_4 = -1{\cdot}0$ V, $V_5 = -5{\cdot}0$ V.

shows that C_s is eliminated by taking the difference, $\Delta C_{m(1,2)}$, between the values of C_m at bias voltages V_1 and V_2. Thus,

$$\Delta C_{m(1,2)} = C_{d(0)}\{(1 - V_1/\phi)^{-1/n} - (1 - V_2/\phi)^{-1/n}\} \qquad \text{.....(8)}$$

Here it is assumed that V_2 is more negative than V_1 so that $\Delta C_{m(1,2)}$ is positive. Further, $C_{d(0)}$ can be eliminated by taking the ratio, K, of $\Delta C_{m(1,2)}$ and a similar difference, $\Delta C_{m(1,3)}$, between bias voltages V_1 and V_3. If V_1, V_2 and V_3 are fixed, K is a function of ϕ and n alone.

Two ratios, K_a and K_b, are defined as follows:

$$K_a = \frac{\Delta C_{m(1,2)}}{\Delta C_{m(1,3)}} = \frac{(1 - V_1/\phi)^{-1/n} - (1 - V_2/\phi)^{-1/n}}{(1 - V_1/\phi)^{-1/n} - (1 - V_3/\phi)^{-1/n}} \qquad \text{.....(9)}$$

$$K_b = \frac{\Delta C_{m(1,4)}}{\Delta C_{m(1,5)}} = \frac{(1 - V_1/\phi)^{-1/n} - (1 - V_4/\phi)^{-1/n}}{(1 - V_1/\phi)^{-1/n} - (1 - V_5/\phi)^{-1/n}} \qquad \text{.....(10)}$$

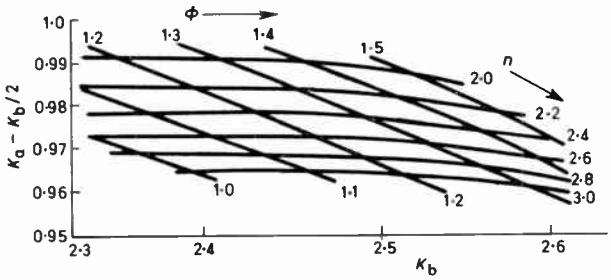

Fig. 4. Chart for the capacitance-voltage parameters of gallium arsenide varactors. $V_1 = -0{\cdot}1$ V, $V_2 = -1{\cdot}25$ V, $V_3 = -0{\cdot}5$ V, $V_4 = -1{\cdot}0$ V, $V_5 = -5{\cdot}0$ V.

If suitable values are chosen for the five bias voltages, then lines of constant ϕ and n can be drawn in the K_a, K_b plane. Values for K_a and K_b are easily found from five capacitance measurements and it is then possible to locate a position in the K_a, K_b plane from which the lines for constant ϕ and n give values for these parameters.

In practice, it is more convenient if a chart is constructed in the $(K_a - K_b/2)$, K_b plane. A chart is shown in Fig. 3 for the indicated values of bias voltage. Provided that the capacitance, C_m, can be measured at the five prescribed bias voltages, this chart can be used for silicon varactors for which $0{\cdot}5 < \phi < 0{\cdot}8$ and $2 < n < 3$. If ϕ and n lie outside these limits, extension of Fig. 3 is necessary. If C_m is measured at another set of five bias voltages, another chart must be constructed. Figure 4 is a similar chart for gallium arsenide varactors and covers the range $1{\cdot}0 < \phi < 1{\cdot}5$ and $2 < n < 3$. Note that it is not necessary for V_1 to be zero and that a small negative value has in fact been used.

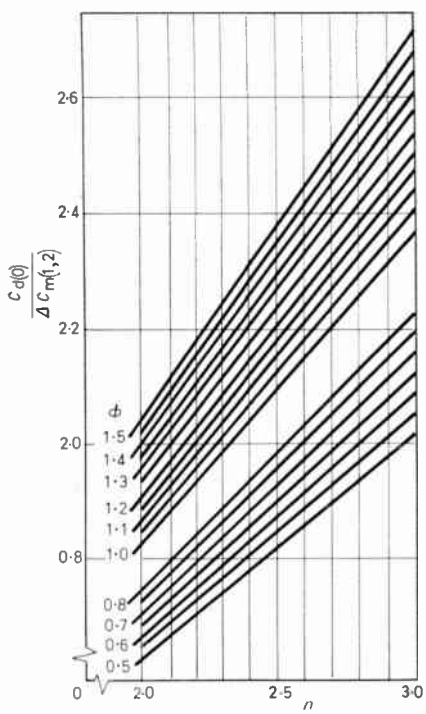

Fig. 5. $C_{d(0)}/\Delta C_{m(1,2)}$ as a function of n with ϕ as a parameter; $V_1 = -0{\cdot}1$, $V_2 = -5{\cdot}0$ V.

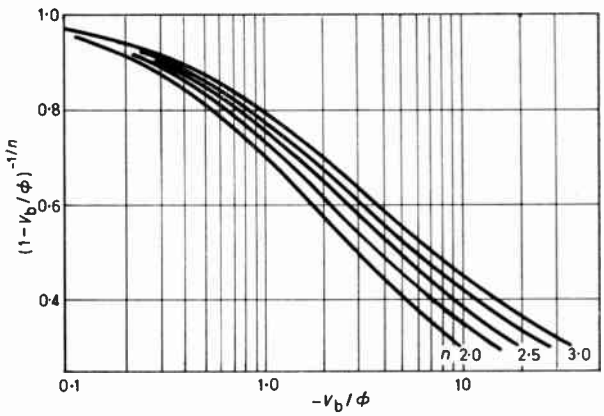

Fig. 6. $(1 - V_b/\phi)^{-1/n}$ as a function of $-V_b/\phi$ with n as a parameter.

Once values for ϕ and n have been determined it is relatively simple to find values for $C_{d(0)}$ and C_s using one of the following methods. In the first method equation (8) is rewritten

$$C_{d(0)}/\Delta C_{m(1,2)} = \{(1 - V_1/\phi)^{-1/n} - (1 - V_2/\phi)^{-1/n}\}^{-1} \quad \ldots\ldots(11)$$

If V_1 and V_2 are fixed, $C_{d(0)}/\Delta C_{m(1,2)}$ is a function of ϕ and n alone. In Fig. 5, $C_{d(0)}/\Delta C_{m(1,2)}$ is plotted as a function of n for a range of values of ϕ, and for $V_1 = -0{\cdot}1$ V and $V_2 = -5{\cdot}0$ V. A value for $C_{d(0)}$ can be found from this graph since the measured change in capacitance $\Delta C_{m(1,2)}$, is known. This graph covers the same range of ϕ and n as the charts of Figs. 3 and 4 and can be used for both silicon and gallium arsenide varactors. It is again only valid for the specified voltages at which capacitance measurements are made. A value for C_s is then found using equation (7).

In the second method C_m is plotted as a function of $(1 - V_b/\phi)^{-1/n}$. This gives a straight line of slope equal to $C_{d(0)}$, and of intercept on the $(1 - V_b/\phi)^{-1/n}$ axis equal to C_s. Since values are known for ϕ and n, values for $C_{d(0)}$ and C_s can be found from a single graph. To enable values for $(1 - V_b/\phi)^{-1/n}$ to be found, this function has been plotted in Fig. 6 as a function of V_b/ϕ for a range of values of n. Figure 7 shows the experimental graph for the silicon varactor, DE2, from which values for $C_{d(0)}$ and C_s shown in Table 1 were found. This method serves as a check on the values found for ϕ and n since a straight line will only be obtained if the values for these are correct.

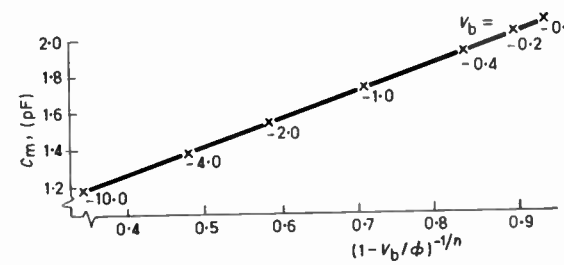

Fig. 7. C_m as a function of $(1 - V_b/\phi)^{-1/n}$ for the silicon varactor, DE2, for which $n = 2{\cdot}6$ and $\phi = 0{\cdot}7$ V.

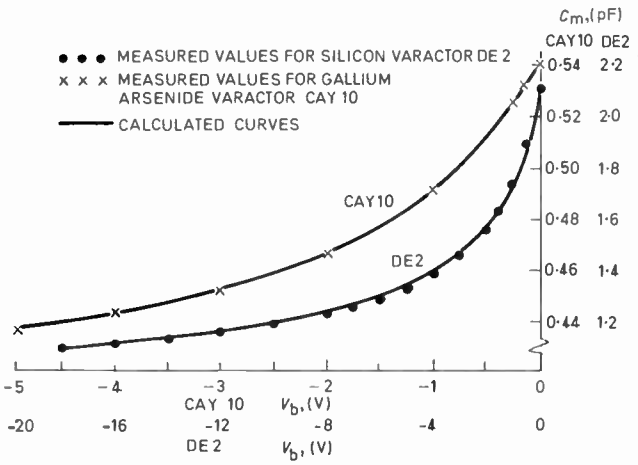

Fig. 8. Comparison of the measured capacitance-voltage relationship and that calculated from the parameters found using the new technique.

In Table 1, the values obtained for the capacitance-voltage parameters of a silicon varactor, DE2, using the new technique are compared with values found by other techniques. Figure 8 is a graph of the capacitance-voltage relationship and shows measured values and the curve calculated from the parameters found using the new technique. Similar results for a gallium arsenide varactor, CAY10, are shown in Table 2 and Fig. 8.

Table 1

Comparison of values for capacitance-voltage parameters for silicon varactor, DE2

Method	$C_{d(0)}$ (pF)	ϕ (volts)	n	C_s (pF)
Reference 4	1·46	0·70	2·3	0·72
Reference 5	1·50	0·65	2·5	0·68
Reference 3	1·51	0·71	2·5	0·67
New technique	1·50	0·70	2·6	0·68

Table 2

Comparison of values for capacitance-voltage parameters for gallium arsenide varactor, CAY10

Method	$C_{d(0)}$ (pF)	ϕ (volts)	n	C_s (pF)
Reference 3	0·232	1·04	2·85	0·309
New technique	0·235	1·00	3·0	0·307

The curves of Fig. 8 show that there is very good agreement between the measured capacitance and the curve calculated from the values of $C_{d(0)}$, C_s, ϕ and n. The difference is less than 2·5% over the whole range of bias voltage.

4. Capacitance Measurement

Measurement of capacitance was made using the transformer ratio-arm bridge, Wayne–Kerr type B201. The transformer windings formed part of the bias circuit but carried a negligible current. Satisfactory results using the methods discussed in Section 3 can only be obtained if the measured capacitance is the true small-signal capacitance.

If the voltage across the varactor is too large, the varactor is voltage pumped and the varactor current is then

$$i = (\omega V_p/2)\{(2C_0 - C_2)\sin \omega t + (C_1 - C_3)\sin 2\omega t + \\ + (C_2 - C_4)\sin 3\omega t + \ldots\} \quad \ldots\ldots(12)$$

Here C_0 is the average capacitance and C_k is the kth capacitance coefficient (see Section 7). V_p is the pump voltage amplitude. The fundamental component is selected by the detector and higher order terms can therefore be neglected. The measured capacitance is equal to the sum of $(C_0 - C_2/2)$ and C_s and this must be compared with $(C_d + C_s)$. The capacitance coefficients C_0 and C_2 can be calculated for a given pump voltage amplitude, V_p, and direct bias voltage, V_b, if the parameters $C_{d(0)}$, ϕ and n of the varactor are known or assumed. This calculation is discussed in Section 5.

Figure 9 shows the percentage error in the measured value of C_d as a function of the pump amplitude coefficient β with the exponent n as a parameter. In calculating this error ϕ was assumed to be 0·6 V, a value typical for silicon varactors. It follows from Fig. 9 that to keep the error below 1% for $n = 2$, the voltage across the varactor must be below 135 mV r.m.s. at $V_b = 0$ the worst condition. Experiment showed that for the varactors used, the signal level should be below 100 mV r.m.s. for true small-signal conditions. However, to obtain high accuracy and discrimination using the transformer ratio-arm bridge, much larger signal levels are conventionally used. So that accuracy and discrimination were not degraded by low signal levels, a very sensitive detector system was necessary. This comprised a communication receiver, with a very narrow i.f. bandwidth to reduce noise, the i.f. output of which was detected by a sensitive heterodyne voltmeter. In this

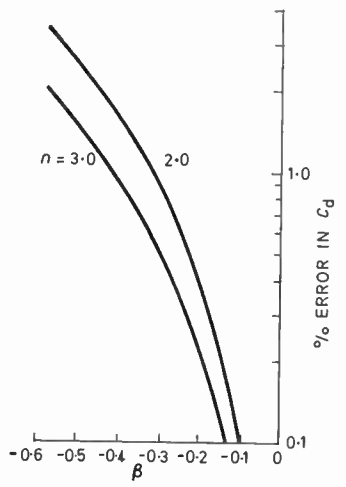

Fig. 9. Percentage error in measured capacitance, C_d, as a function of the pumping coefficient, β.

$$\%\ \text{error} = \frac{(C_0 - C_2/2) - C_d}{C_d}\ 100,\ \beta = -\frac{V_b}{\phi - V_b} \quad \ldots\ldots(13)$$

way a very high gain detector was realized which had a very narrow noise bandwidth. This enabled a resolution of $\pm 0{\cdot}1\%$ to be obtained on the measurement of a capacitance of 1·0 pF. In capacitance measurement, for all the methods discussed resolution was more important than absolute accuracy since changes in capacitance are used.

5. Determination of the Parameters of the Pumped Varactor

If values for $C_{d(0)}$, ϕ and n are available and the pump waveform is known, it is possible to determine values for the parameters C_0 and γ_k, of the pumped varactor. An analytical solution is only possible for the restricted cases when the voltage across or the current through the depletion-layer capacitance is sinusoidal,[8] i.e. for voltage or current pumping. The determination of values for C_0 and γ_k (for $k = 1$, 2 and 3) from the values of $C_{d(0)}$, ϕ and n will now be considered for voltage and current pumping.

5.1. *Voltage Pumping*

The pump voltage across the depletion-layer capacitance is

$$v = V_b + V_p \cos(\omega_p t) \qquad \text{.....(14)}$$

Substitution into equation (7) expresses the depletion-layer capacitance as a function of time. Thus

$$C(t) = C_{db}\left(1 - \frac{V_p}{\phi - V_b}\cos(\omega_p t)\right)^{-1/n} \qquad \text{.....(15)}$$

where C_{db} is the depletion-layer capacitance at the d.c. bias voltage, V_b.

If equation (15) is expanded as a Fourier series the coefficients C_0 and γ_k are given by

$$C_0 = \frac{1}{2\pi}\int_0^{2\pi} C(t)\,\mathrm{d}(\omega_p t) \qquad \text{.....(16)}$$

and

$$\gamma_k = \frac{1}{2\pi C_0}\int_0^{2\pi} C(t)\cos(k\omega_p t)\,\mathrm{d}(\omega_p t) \qquad \text{.....(17)}$$

Hence

$$C_0 = \frac{1}{2\pi}C_{db}\int_0^{2\pi}\left(1 - \frac{V_p}{\phi - V_b}\cos(\omega_p t)\right)^{-1/n}\mathrm{d}(\omega_p t) \qquad \text{...(18)}$$

and

$$\gamma_k = \frac{1}{2\pi}\frac{C_{db}}{C_0}\int_0^{2\pi}\left(1 - \frac{V_p}{\phi - V_b}\cos(\omega_p t)\right)^{-1/n} \times \cos(k\omega_p t)\,\mathrm{d}(\omega_p t) \qquad \text{.....(19)}$$

The solution of equations (18) and (19) is relatively straightforward for an ideal abrupt junction ($n = 2$), and an ideal linearly-graded junction ($n = 3$).[8] However, the experimentally-determined value for n generally lies in the range $2 < n < 3$ and solution becomes difficult[9,10] involving the evaluation of a hypergeometric function.

5.2. *Current Pumping*

In the case of current pumping, the current through the diode varies sinusoidally with time. Thus the time variation of charge on the p-side of the junction is also sinusoidal and can be written

$$Q_i = Q_b + Q_p \cos(\omega_p t) \qquad \text{.....(20)}$$

Here Q_b is the injected charge associated with the d.c. bias voltage V_b, and from equation (5),

$$Q_b = -Q_{d(0)}\{(1 - V_b/\phi)^{(n-1)/n} - 1\} \qquad \text{.....(21)}$$

The depletion-layer capacitance can again be expressed as a time-dependent function. Equation (20) is substituted into equation (6) giving

$$C(t) = C_{db}\left(1 - \frac{Q_p}{Q_{d(0)} - Q_b}\cos(\omega_p t)\right)^{-1/(n-1)} \qquad \text{.....(22)}$$

Thus for current pumping it follows that values for C_0 and γ_k can be found by the solution of the integrals:

$$C_0 = \frac{1}{2\pi}C_{db}\int_0^{2\pi}\left(1 - \frac{Q_p}{Q_{d(0)} - Q_b}\cos(\omega_p t)\right)^{-1/(n-1)}\mathrm{d}(\omega_p t) \qquad \text{.....(23)}$$

and

$$\gamma_k = \frac{1}{2\pi}\frac{C_{db}}{C_0}\int_0^{2\pi}\left(1 - \frac{Q_p}{Q_{d(0)} - Q_b}\cos(\omega_p t)\right)^{-1/(n-1)} \times \cos(k\omega_p t)\,\mathrm{d}(\omega_p t) \qquad \text{.....(24)}$$

5.3. *Charts for the Determination of Values for C_0 and γ_k*

Comparison of equations (18) and (23) shows that the expression for C_0 is of the same form for voltage and current pumping and can be written in a general way as

$$C_0 = \frac{1}{2\pi}C_{db}\int_0^{2\pi}\{1 + \beta\cos(\omega_p t)\}^{\alpha}\,\mathrm{d}(\omega_p t) \qquad \text{.....(25)}$$

Similarly, comparison of equations (19) and (24) shows that the expression for γ_k can be written

$$\gamma_k = \frac{1}{2\pi}\frac{C_{db}}{C_0}\int_0^{2\pi}\{1 + \beta\cos(\omega_p t)\}^{\alpha}\cos(k\omega_p t)\,\mathrm{d}(\omega_p t) \qquad \text{.....(26)}$$

In the last two equations, α is termed the generalized junction exponent and β the pump amplitude coefficient. These are defined in Table 3 for voltage and current pumping.

Table 3

Definitions for α and β for voltage and current pumping

	Voltage pumping	Current pumping
α	$-\frac{1}{n}$	$-\frac{1}{n-1}$
β	$-\frac{V_p}{\phi - V_b}$	$-\frac{Q_p}{Q_{d(0)} - Q_b}$

Penfield[9,10] has defined the integral

$$I(\alpha, k; \beta) = \frac{1}{2\pi}\int_0^{2\pi}(1 + \beta\cos\theta)^{\alpha}\cos(k\theta)\,\mathrm{d}\theta \qquad \text{.....(27)}$$

where $k = 0$, 1, 2, 3, etc.

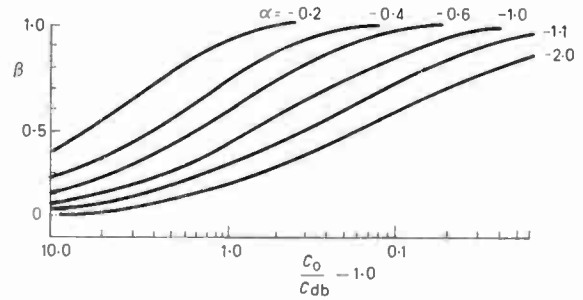

Fig. 10. Chart for the average capacitance coefficient ($C_0/C_{db}-1$) as plotted as a function of β with α as a parameter. C_0 is the zero-order capacitance coefficient, and C_{db} is the capacitance at the d.c. bias voltage V_b.

A computer program subroutine was written to solve equation (27). The subroutine has been used to construct charts from which the coefficients C_0, γ_1, γ_2 and γ_3 can be found and these are shown in Figs. 10, 11, 12 and 13 respectively. A separate chart is necessary for each coefficient but each chart is valid for both voltage and current pumping. Although charts can be constructed for high-order coefficients, these can generally be neglected except under exceptional circumstances.

To illustrate the use of these generalized charts and to assess their validity, they were used to find the values of the capacitance coefficients for experimental varactors, for which values of $C_{d(0)}$, ϕ and n had been determined. Figures 14 and 15 show the capacitance coefficients expressed as functions of pump voltage amplitude. The coefficients shown in these curves have been checked by graphical analysis from the measured capacitance-voltage relationship and by direct measurement. C_0' and C_k are related to C_0 and γ_k by

$$C_0' = C_0 + C_S \qquad \text{.....(28)}$$

and

$$C_k = 2\gamma_k C_0 \qquad \text{.....(29)}$$

6. Graphical Determination of Values for C_0 and γ_k

For a fixed bias voltage, the pump voltage waveform was sampled over the range of $\omega_p t$ from 0 to 2π, and the corresponding instantaneous capacitance values were obtained from the measured capacitance-voltage curve. Sufficient accuracy was obtained with 40 samples of

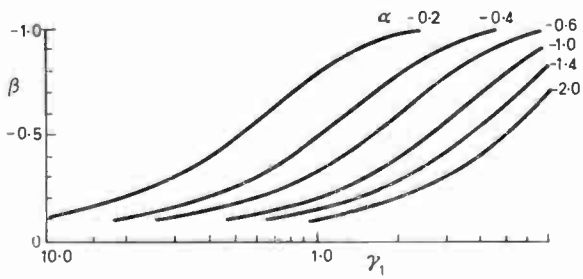

Fig. 11. Chart for the fundamental or first-order γ-coefficient, γ_1.

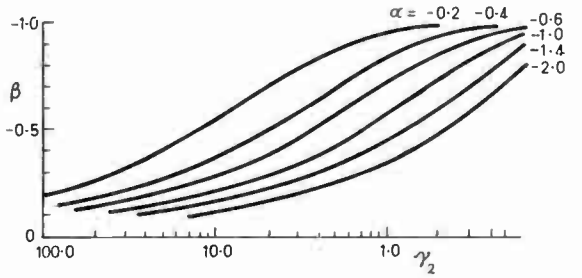

Fig. 12. Chart of the second-order γ-coefficient, γ_2.

equal increments of $\omega_p t$. Numerical methods of harmonic analysis were then used to find the capacitance coefficients.[11] This was repeated for three values of pump voltage amplitude.

7. Experimental Determination of the Values for C_0 and γ_k

Measurement of the coefficients C_0', C_1, C_2 and C_3 was made at a frequency of 0·1 MHz, since at this frequency sinusoidal voltage pumping was possible. Accurate measurement of the harmonic content of the resulting current could also be made and from this values for the capacitance coefficients were determined.

For sinusoidal voltage pumping, the current through the depletion-layer capacitance can be shown to be,

$$i(t) = -\frac{\omega_p V_p}{2}\{(2C_0' - C_2)\sin\omega_p t + (C_1 - C_3)\sin 2\omega_p t + (C_2 - C_4)\sin 3\omega_p t + \ldots\} \qquad \text{.....(30)}$$

but

$$i(t) = I_1 \sin\omega_p t + I_2 \sin 2\omega_p t + \ldots \qquad \text{.....(31)}$$

where I_1, I_2, etc. are the harmonic coefficients of the current, and these can be measured. The capacitance coefficients are therefore given by

$$C_0' = \frac{1}{\omega_p V_p}(I_1 + I_3 + I_5 + \ldots) \qquad \text{.....(32)}$$

and

$$C_k = \frac{2}{\omega_p V_p}(I_{k+1} + I_{k+3} + I_{k+5} + \ldots) \qquad \text{.....(33)}$$

The magnitudes of the harmonic currents were found by measuring the corresponding harmonic voltage across the 1 kΩ precision sampling resistor in series with the varactor. This resistance was much smaller than

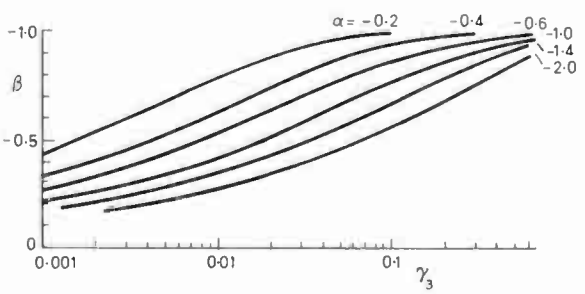

Fig. 13. Chart for the third-order γ-coefficient, γ_3.

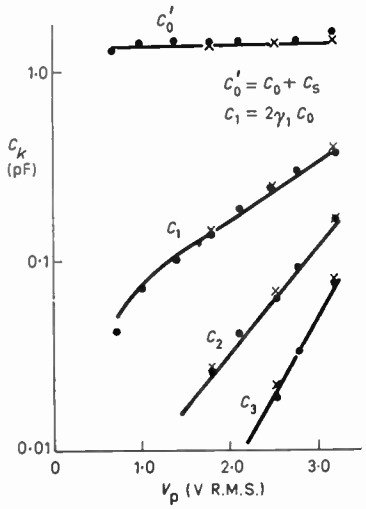

Fig. 14. Comparison of the capacitance coefficients of a voltage pumped silicon varactor, DE2 ($V_b = -4{\cdot}5$ V). The continuous line shows the calculated values (Sect. 5), graphically determined values (Sect. 6) are shown by crosses and measured values (Sect. 7) are shown by dots.

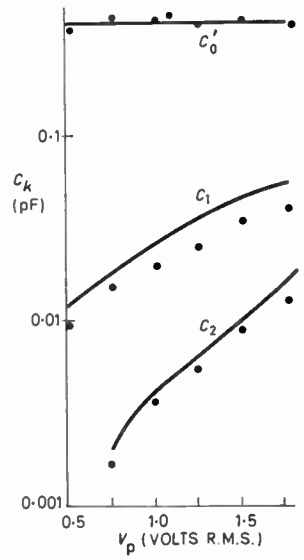

Fig. 15. Comparison of capacitance coefficients of voltage pumped gallium arsenide varactor, CAY 10 ($V_b = -2{\cdot}5$ V). The continuous line shows the calculated values (Sect. 5), and the measured values (Sect. 7) are shown by dots.

the capacitive reactance of the varactor and hence the waveform of the voltage across the varactor was therefore unaffected. Values of C_0', C_1, C_2 and C_3, obtained by this experimental method for a range of pump voltage amplitudes are compared in Figs. 14 and 15, with the values obtained by calculation from $C_{d(0)}$, ϕ, n and C_s using the method of Section 5, and with the values obtained using the graphical method of Section 6.

8. Conclusions

A new technique for the determination of the parameters $C_{d(0)}$, ϕ, n and C_s, of the varactor capacitance-voltage relationship has been proposed. This is compared with two other methods previously proposed by the authors, and is found to be superior in two ways. Firstly, in determining values for ϕ and n accurate measurement of capacitance at only five bias voltages is required and secondly the slope of the capacitance-voltage relationship does not have to be determined. Experimental results are presented and there is good agreement between calculated and measured capacitance values. The parameters are then used in the determination of the capacitance coefficients of the pumped varactor. Charts of the capacitance coefficients are presented as functions of the parameters, for both voltage and current pumping. The charts are used to determine the capacitance coefficients of a voltage-pumped varactor, and the values compared with results found graphically and by experiment. The parameters of the capacitance-voltage relationship and the capacitance coefficients of the pumped varactor were determined at frequencies of 1·0 MHz and 0·1 MHz respectively, but the results should be applicable over the range of frequencies for which the capacitance-voltage relationship is valid.

9. References

1. Blackwell, L. A. and Kotzebue, K. L., 'Semiconductor-diode Parametric Amplifiers' (Prentice Hall, Englewood Cliffs, N.J., 1961).
2. Howson, D. P. and Smith, R. B., 'Parametric Amplifiers' (McGraw-Hill, London, 1970).
3. Bajon, J., Hoffman, J. C. and Hait, J. R., 'Method dealing with the experimental determination of the hyper-abrupt junction varactor characteristics', *Electronics Letters*, **5**, pp. 132–4, 3rd April 1969 (in French).
4. Hyde, F. J., Deval, S. and Toker, C., 'Varactor diode measurements', *The Radio and Electronic Engineer*, **31**, pp. 67–75, February 1966.
5. Smith, R. B., Bramer, B. and Croft, D. G., 'Determination of the constants of the capacitance/voltage law of the varactor diode', *Electronics Letters*, **4**, pp. 274–5, 28th June 1968.
6. Hyde, F. J., 'Semiconductors' (Macdonald, London, 1965).
7. Nuyts, W. and Van Overstraeten, R. J., 'Numerical calculations of the capacitance of linearly graded Si p-n junctions', *Electronics Letters*, **5**, pp. 54–5, 6th February 1969.
8. Penfield, P. (Jr.) and Rafuse, R. P., 'Varactor Applications' (The M.I.T. Press, Cambridge, Mass., 1962).
9. Penfield, P. (Jr.), 'Fourier coefficients of power law devices', *J. Franklin Inst.*, **273**, pp. 107–22, February 1962.
10. Penfield, P., 'Tables and Formulae for Calculating Fourier Coefficients of Power Law Devices', Tech. Report No. 385, M.I.T. Research Lab. of Electronics, 20th March 1963.
11. Golding, E. W. and Widdis, F. C., 'Electrical Measurements and Measuring Instruments' (Pitman, London, 1963).

Manuscript first received by the Institution on 26th January 1970, in revised form on 18th February 1972, and in final form on 6th April 1972. (Paper No. 1469/CC 145.)

Contributors to this issue

Dr. B. Bramer received his undergraduate and postgraduate training at Bradford University, where he obtained a B.Tech. honours degree in 1967, and in 1971 was awarded a Ph.D. for work on the determination of the properties of varactor diodes. He is at present an SRC Experimental Officer in the School of Electrical Engineering at Bath University, where he is working on computer-graphics-aided synthesis of electronic circuits for signal processing purposes.

Mr. B. O. Baker graduated from Imperial College, London, in 1943, and joined the Valve Division of the G.E.C. Hirst Research Centre at Wembley. He spent 14 years in the Receiving Valve Group, and 14 years in the Gas-filled Valve Group where the development work on the laser was carried out. In 1971 he transferred to the M-O Valve Company at Hammersmith, where he is responsible for the technical aspects of telephone surge arresters.

Dr. R. B. Smith trained as an apprentice with the Marconi Company and subsequently received a B.Sc. honours degree in 1959 and a Ph.D. in 1964 at the University College of North Wales, Bangor. He then worked for two years at Marconi College, Chelmsford, where he was concerned with postgraduate training. Since 1965 he has been at Bradford University as a Lecturer and then Senior Lecturer, and his present research interests are in microwave solid-state devices and industrial applications of microwaves.

Mr. D. W. E. Fuller graduated from London University with a B.Sc. degree in special physics in 1955. After working with Electronic Instruments Ltd. and M-O Valve Co. he was appointed Chief Engineer of Solus Electronic Tubes in 1959. His investigations into breakdown in gases led to an M.Sc. in 1966. Since 1967 he has been at the National Physical Laboratory where lasers he has developed are used for measurements at sub-millimetre wavelengths. Currently he is engaged in the precision measurement of power.

Mr. D. G. Haigh obtained a B.Sc. degree in electrical engineering at the University of Bristol in 1968. Until recently he has worked in the Circuit Theory Group at the G.E.C. Hirst Research Centre, studying active networks. He is now continuing this work in the Electrical Engineering Department of the Imperial College of Science and Technology.

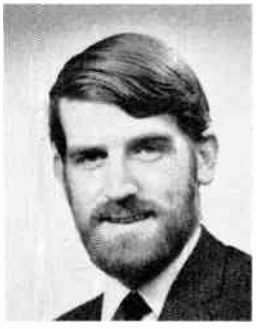

Mr. R. Jeffers obtained a B.Sc. degree in electrical engineering at the Queen's University of Belfast in 1966. Since 1967 he has worked in the Circuit Theory Group at the G.E.C. Hirst Research Centre, studying active and time-varying networks. He has recently joined a group at the Hirst Research Centre working on computer-aided design.